PHYSICAL REVIEW D **78,** 052001 (2008)

Dalitz plot analysis of the $D^+ \to K^-\pi^+\pi^+$ decay

G. Bonvicini,[1] D. Cinabro,[1] M. Dubrovin,[1] A. Lincoln,[1] P. Naik,[2] J. Rademacker,[2] D. M. Asner,[3] K. W. Edwards,[3] J. Reed,[3] R. A. Briere,[4] T. Ferguson,[4] G. Tatishvili,[4] H. Vogel,[4] M. E. Watkins,[4] J. L. Rosner,[5] J. P. Alexander,[6] D. G. Cassel,[6] J. E. Duboscq,[6] R. Ehrlich,[6] L. Fields,[6] L. Gibbons,[6] R. Gray,[6] S. W. Gray,[6] D. L. Hartill,[6] B. K. Heltsley,[6] D. Hertz,[6] J. M. Hunt,[6] J. Kandaswamy,[6] D. L. Kreinick,[6] V. E. Kuznetsov,[6] J. Ledoux,[6] H. Mahlke-Krüger,[6] D. Mohapatra,[6] P. U. E. Onyisi,[6] J. R. Patterson,[6] D. Peterson,[6] D. Riley,[6] A. Ryd,[6] A. J. Sadoff,[6] X. Shi,[6] S. Stroiney,[6] W. M. Sun,[6] T. Wilksen,[6] S. B. Athar,[7] R. Patel,[7] J. Yelton,[7] P. Rubin,[8] B. I. Eisenstein,[9] I. Karliner,[9] S. Mehrabyan,[9] N. Lowrey,[9] M. Selen,[9] E. J. White,[9] J. Wiss,[9] R. E. Mitchell,[10] M. R. Shepherd,[10] D. Besson,[11] T. K. Pedlar,[12] D. Cronin-Hennessy,[13] K. Y. Gao,[13] J. Hietala,[13] Y. Kubota,[13] T. Klein,[13] B. W. Lang,[13] R. Poling,[13] A. W. Scott,[13] P. Zweber,[13] S. Dobbs,[14] Z. Metreveli,[14] K. K. Seth,[14] A. Tomaradze,[14] J. Libby,[15] A. Powell,[15] G. Wilkinson,[15] K. M. Ecklund,[16] W. Love,[17] V. Savinov,[17] A. Lopez,[18] H. Mendez,[18] J. Ramirez,[18] J. Y. Ge,[19] D. H. Miller,[19] I. P. J. Shipsey,[19] B. Xin,[19] G. S. Adams,[20] M. Anderson,[20] J. P. Cummings,[20] I. Danko,[20] D. Hu,[20] B. Moziak,[20] J. Napolitano,[20] Q. He,[21] J. Insler,[21] H. Muramatsu,[21] C. S. Park,[21] E. H. Thorndike,[21] F. Yang,[21] M. Artuso,[22] S. Blusk,[22] S. Khalil,[22] J. Li,[22] R. Mountain,[22] S. Nisar,[22] K. Randrianarivony,[22] N. Sultana,[22] T. Skwarnicki,[22] S. Stone,[22] J. C. Wang,[22] and L. M. Zhang[22]

(CLEO Collaboration)

[1]*Wayne State University, Detroit, Michigan 48202, USA*
[2]*University of Bristol, Bristol BS8 1TL, United Kingdom*
[3]*Carleton University, Ottawa, Ontario, Canada K1S 5B6*
[4]*Carnegie Mellon University, Pittsburgh, Pennsylvania 15213, USA*
[5]*Enrico Fermi Institute, University of Chicago, Chicago, Illinois 60637, USA*
[6]*Cornell University, Ithaca, New York 14853, USA*
[7]*University of Florida, Gainesville, Florida 32611, USA*
[8]*George Mason University, Fairfax, Virginia 22030, USA*
[9]*University of Illinois, Urbana-Champaign, Illinois 61801, USA*
[10]*Indiana University, Bloomington, Indiana 47405, USA*
[11]*University of Kansas, Lawrence, Kansas 66045, USA*
[12]*Luther College, Decorah, Iowa 52101, USA*
[13]*University of Minnesota, Minneapolis, Minnesota 55455, USA*
[14]*Northwestern University, Evanston, Illinois 60208, USA*
[15]*University of Oxford, Oxford OX1 3RH, United Kingdom*
[16]*State University of New York at Buffalo, Buffalo, New York 14260, USA*
[17]*University of Pittsburgh, Pittsburgh, Pennsylvania 15260, USA*
[18]*University of Puerto Rico, Mayaguez, Puerto Rico 00681*
[19]*Purdue University, West Lafayette, Indiana 47907, USA*
[20]*Rensselaer Polytechnic Institute, Troy, New York 12180, USA*
[21]*University of Rochester, Rochester, New York 14627, USA*
[22]*Syracuse University, Syracuse, New York 13244, USA*
(Received 27 February 2008; published 10 September 2008)

We perform a Dalitz plot analysis of $D^+ \to K^-\pi^+\pi^+$ decay with the CLEO-c data set of 572 pb^{-1} of e^+e^- collisions accumulated at the $\psi(3770)$. This corresponds to 1.6×10^6 D^+D^- pairs from which we select 140 793 candidate events with a small background of 1.1%. We compare our results with previous measurements using the isobar model. We modify the isobar model with an improved description of some of the contributing resonances and get better agreement with our data. We also consider a quasi-model-independent approach and measure the magnitude and phase of the contributing $K\pi$ S wave in the range of invariant masses from the threshold to the maximum in this decay. This gives an improved description of our data over the isobar model. Finally we allow for an isospin-two $\pi^+\pi^+$ S wave contribution and find that adding this to both the isobar model and the quasi-model-independent approach gives the best description of our data.

DOI: 10.1103/PhysRevD.78.052001 PACS numbers: 11.80.Et, 13.25.−k, 13.25.Ft, 14.40.Lb

I. INTRODUCTION

In comparison to other D^+ decay modes, the $D^+ \to K^-\pi^+\pi^+$ decay is unique in many aspects. The large branching fraction $\mathcal{B}(D^+ \to K^-\pi^+\pi^+) = (9.51 \pm 0.34)\%$ [1] for this Cabibbo favored mode makes it the usual choice for normalization of other D^+-meson decay rates. Understanding its peculiar intermediate substructure will be beneficial. The only obvious contribution to this decay, observed in the $K\pi$-mass spectrum, is $K^*(892)^0\pi^+$, which comprises merely 12% of the total rate [1]. A large contribution of over 60% from a $K\pi$ S wave intermediate state has been observed in earlier experiments, including MARK III [2], NA14 [3], E691 [4], E687 [5], and E791 [6,7], where the $D^+ \to K^-\pi^+\pi^+$ decay has been studied with the Dalitz plot technique [8]. Hence, the $D^+ \to K^-\pi^+\pi^+$ decay is a good laboratory to study $K\pi$ S wave dynamics.

The previous analysis by E791 [6] achieved good agreement with their data by including a low-mass $K^-\pi^+$ scalar resonance κ that significantly redistributed all fit fractions (FF) observed by earlier experiments. This particular model, even though it is based on the largest data set, greatly disagrees with previous analyses and has been excluded from the average given by the Particle Data Group (PDG) [1].

There has been significant theoretical interest in this decay, sparked by the large, low-mass $K\pi$ S wave contribution. In Refs. [9–11] the authors reanalyze the E791 data with their own models. E791 later reinterpreted their own data with a model-independent partial wave analysis [7], and we apply this in our analysis with minor modifications.

The two identical pions in the final state should obey Bose symmetry. Assuming that the three-body decay is dominated by two-body intermediate states, there would be two identical $K^-\pi^+$ waves interfering with each other. This twofold symmetry significantly reduces the degrees of freedom in the regular Dalitz plot analysis and allows the application of a model-independent partial wave analysis [7]. We would also expect a small contribution from the isospin-two $\pi^+\pi^+$ S wave, which exhibits nontrivial dynamics as observed in scattering experiments [12].

The data used in this analysis were accumulated with the CLEO-c detector [13]. Our event sample is based on 572 pb^{-1} of e^+e^- collisions at $\sqrt{s} \approx 3774$ MeV, produced by the Cornell Electron Storage Ring (CESR). This sample corresponds to the production of 1.6×10^6 D^+D^- pairs in the process $e^+e^- \to \psi(3770) \to D^+D^-$. We select 140 793 $D^+ \to K^-\pi^+\pi^+$ candidates for the Dalitz plot analysis (charge conjugation is implied throughout this paper). Our sample is very clean with a background fraction of about 1.1% and is 9 times larger than the data set used by E791. The invariant mass resolution in this three-track D-meson decay is very good; we estimate it is better than 5 MeV/c^2 in most cases. It is improved by a kinematic fit requiring a three-track common vertex with the D-meson mass constraint. Our kinematic conditions are similar to those of MARK III, where D mesons are produced with small momentum.

In Sec. II we briefly discuss CLEO-c experimental techniques, giving the event selection for the Dalitz plot analysis, the general fit method and methods to parametrize the signal efficiency and background distribution across the Dalitz plot. The formalism we use for the amplitude parametrization in this analysis is described in Sec. III. In Sec. IV we compare our results with the best previous measurements by E791 [6] and try to improve the isobar model in order to get a better description of our data. Finally, we apply a quasi-model-independent partial wave analysis, following Ref. [7] and measure the partial waves contributing to this decay in Sec. V. Systematic studies and cross-checks are considered in Sec. VI. We discuss results and outstanding issues of this analysis in Sec. VII and summarize our results in Sec. VIII. In the appendix we discuss the kinematic variables and angular distributions used in this analysis.

II. DETECTOR AND EXPERIMENTAL TECHNIQUE

A. Detector

CLEO-c is a general purpose detector which includes a tracking system for measuring momenta and specific ionization of charged particles, a ring imaging Cherenkov detector to aid particle identification, and a CsI calorimeter for detection of electromagnetic showers. These components are immersed in a magnetic field of 1 T, provided by a superconducting solenoid, and surrounded by a muon detector. The CLEO-c detector is described in detail elsewhere [13].

B. Event reconstruction

We reconstruct the $D^+ \to K^-\pi^+\pi^+$ decay using three tracks measured in the tracking system. Charged tracks satisfy standard goodness of fit quality requirements [14]. Pion and kaon candidates are required to have specific ionization dE/dx in the main drift chamber within 4 standard deviations of the expected value at the measured momentum.

In order to select $D^+ \to K^-\pi^+\pi^+$ decays, we use two kinematic variables

$$\Delta E = E_D - E_{\text{beam}}, \tag{1}$$

$$m_{\text{BC}} = \sqrt{E^2_{\text{beam}} - \text{P}^2_D}, \tag{2}$$

where E_{beam} is the beam energy and E_D and P_D are the energy and the magnitude, respectively, of the momentum of the reconstructed D^+ candidate. The m_{BC} and $|\Delta E|$ two-dimensional distribution and the projections for data are shown in Fig. 1. The resolutions in ΔE and m_{BC} are represented as $\sigma(\Delta E) = 6\,\text{MeV}$ and $\sigma(m_{\text{BC}}) = 1.5\,\text{MeV}/c^2$,

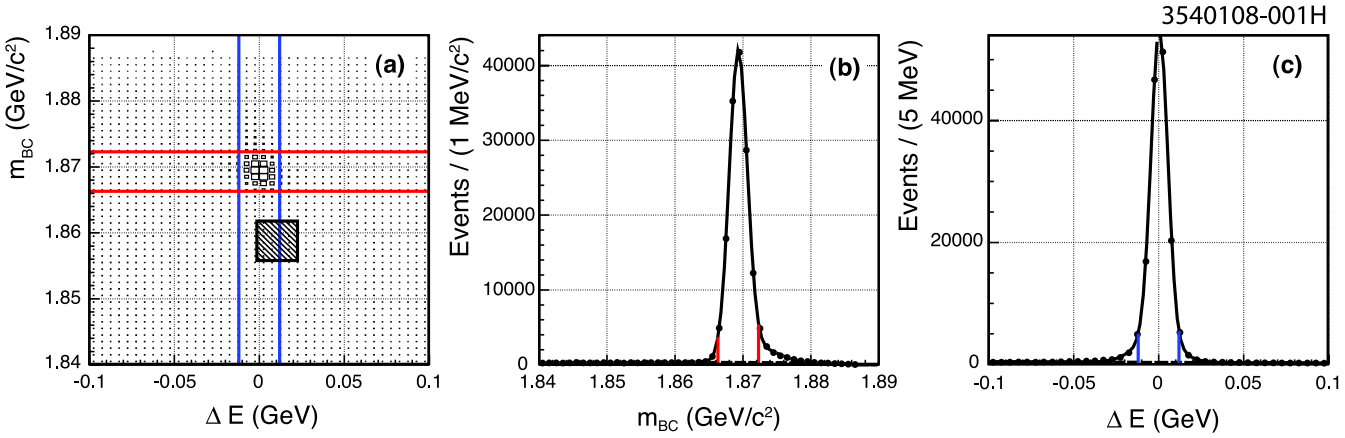

FIG. 1 (color online). Event selection. (a) The $m_{\rm BC}$ and $|\Delta E|$ two-dimensional distribution for data and the projections on (b) $m_{\rm BC}$ and (c) ΔE. The $m_{\rm BC}$ and ΔE signal regions, defined in the text, are shown as the bands in the figures. In (a), the "signal box" is indicated as the crossing area of the two bands while the "sideband box," defined in the text, is indicated as the shaded rectangle. Each projection is made with the events in the signal region of the other kinematic variable; the fit curve, described in the text, is also shown.

respectively; fits with a Gaussian function to the ΔE and $m_{\rm BC}$ peaks evaluate the resolutions to be 5.539 ± 0.014 MeV and 1.410 ± 0.013 MeV/c^2, respectively. We require the events to fall in the "signal box" that is the overlap region of the ΔE and $m_{\rm BC}$ signal regions defined as $|\Delta E| < 2\sigma(\Delta E)$ and $|m_{\rm BC} - m_D| < 2\sigma(m_{\rm BC})$, respectively. In the case of multiple D-meson candidates per event we select the one with the smallest $|\Delta E|$ value.

The $K^-\pi^+\pi^+$ final state has two identical π^+ mesons. To account for this symmetry we analyze events on the Dalitz plot by choosing $x = m^2(K^-\pi^+)_{\rm low}$ and $y = m^2(K^-\pi^+)_{\rm high}$ as the independent (x, y) variables. This choice folds all of the data onto the top half of the kinematically allowed region, as is shown in Fig. 2(a). The third variable $z = m^2(\pi^+\pi^+)$ is dependent on x and y through energy and momentum conservation. The invariant mass resolutions, propagated from the track error matrices, are shown in Fig. 3 and in 95% of cases are better than 5 MeV/c^2. We use a kinematic fit to all 3-track candidates which enforces a common vertex and D^+ mass [1] constraint. We require that all events pass the kinematic fit successfully but do not restrict their χ^2. The kinematic-fit-corrected 4-momenta of all 3 particles are used to calculate invariant masses for further Dalitz plot analysis. Within its finite accuracy, the kinematic fit improves the $K^-\pi^+\pi^+$ invariant mass resolution by 2 orders of magnitude. Proportional improvement is expected for all two-body invariant mass resolutions.

After all requirements, we select 140 793 events for the Dalitz plot analysis. The signal fraction in this sample $f_{\rm sig}$ is estimated to be $(98.917 \pm 0.013)\%$ from the fit to the $m_{\rm BC}$ distribution, shown in Fig. 1(b). In this fit the signal and background shapes are described by the double-Gaussian and ARGUS [15] functions, respectively, with all parameters free. This value of $f_{\rm sig}$ is consistent with one obtained from the fit to ΔE distribution, shown in Fig. 1(c). In most fits to the Dalitz plot we use the fixed value of the signal fraction. Figure 2 shows the Dalitz plot data and two

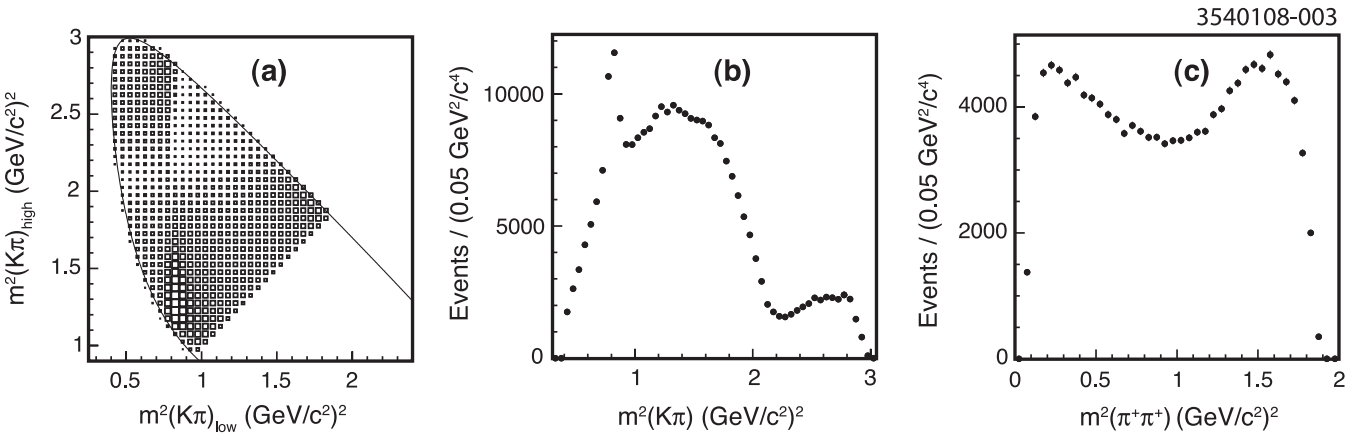

FIG. 2. (a) Dalitz plot for data and their projections on (b) $m^2(K\pi)$ (two entries per event) and (c) $m^2(\pi\pi)$ variables.

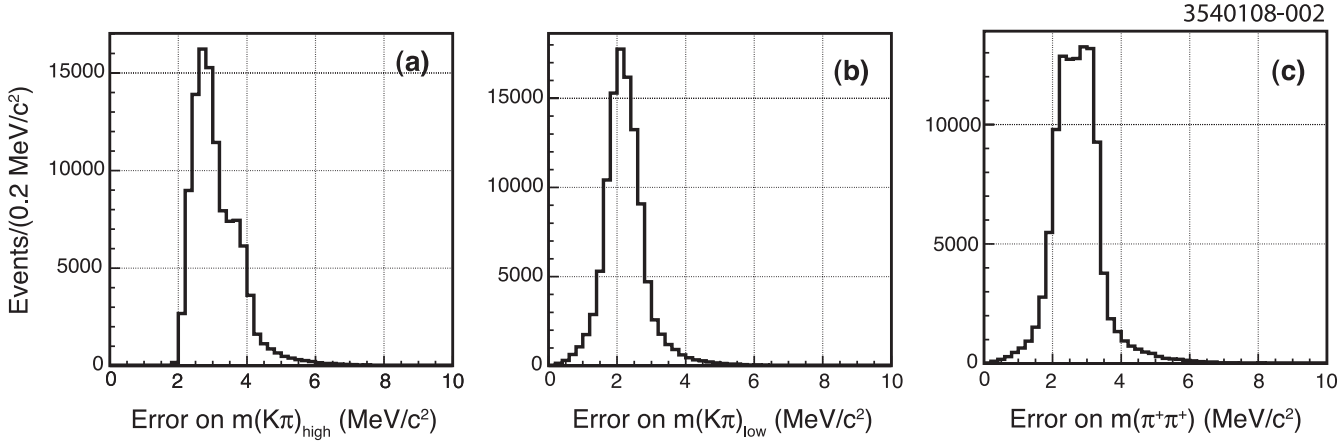

FIG. 3. Invariant mass resolutions before the kinematic fit for (a) $m(K\pi)_{\rm high}$, (b) $m(K\pi)_{\rm low}$, and (c) $m(\pi\pi)$.

projections onto the $m^2(K\pi)$ axes [two entries per event for $m^2(K\pi)_{\rm low}$ and $m^2(K\pi)_{\rm high}$, respectively] and $m^2(\pi\pi)$. Besides the clear $K^*(892)$ signal, no other narrow features are obvious. The strong left-right asymmetry of the $K^*(892)$ population density on the Dalitz plot is evidence of the interference between P and S waves. There are broad structures, including a peak at $m^2(K\pi)$ around 1.3 GeV$^2/c^4$, a dip at $m^2(K\pi)$ around 2.25 GeV$^2/c^4$, a dip at $m^2(\pi\pi)$ around 1 GeV$^2/c^4$, and a peak at $m^2(\pi\pi)$ around 1.6 GeV$^2/c^4$, that do not obviously correspond with known resonances or their reflections from other axes. These structures also do not correspond to a flat phase space distribution for nonresonant decays, since our efficiency is essentially flat across the Dalitz plot, and the background is very low. Thus, we are compelled to consider $K\pi$ strong interaction dynamics to explain the Dalitz plot.

C. Fit method

In order to describe the event density distribution on the Dalitz plot we use a probability density function (p.d.f.) $\mathcal{P}(x, y)$, which depends on the event sample being fit:

$$\mathcal{P}(x,y) = \begin{cases} \mathcal{N}_\varepsilon \varepsilon(x,y) & \text{for efficiency,} \\ \mathcal{N}_B B(x,y) & \text{for background,} \\ f_{\rm sig}\mathcal{N}_S|\mathcal{M}(x,y)|^2\varepsilon(x,y) + (1-f_{\rm sig})\mathcal{N}_B B(x,y) & \text{for signal with background,} \end{cases} \tag{3}$$

where the $\varepsilon(x, y)$ and $B(x, y)$ are the functions representing the shape of the efficiency and background, respectively, across the Dalitz plot. The signal p.d.f. is proportional to the efficiency-corrected matrix element squared $|\mathcal{M}(x, y)|^2$, defined in Sec. III, whose fraction $f_{\rm sig}$ is introduced earlier. The background term has a relative $(1 - f_{\rm sig})$ fraction. All p.d.f. components are normalized separately using the normalization integrals over the Dalitz plot area $1/\mathcal{N}_\varepsilon = \int \varepsilon(x, y)dxdy$, $1/\mathcal{N}_B = \int B(x, y)dxdy$, and $1/\mathcal{N}_S = \int |\mathcal{M}(x, y)|^2\varepsilon(x, y)dxdy$, which provides the overall p.d.f. normalization $\int \mathcal{P}(x, y)dxdy = 1$. The p.d.f. free parameters are optimized with an maximum likelihood fit that minimizes the sum over N events:

$$\mathcal{L} = -2\sum_{n=1}^{N} \log \mathcal{P}(x_n, y_n). \tag{4}$$

To estimate the fit quality we use Pearson's statistics for adaptive bins, similar to our previous analysis [16].

D. Efficiency parametrization

To determine the efficiency we use a signal Monte Carlo (MC) [17] simulation where one of the charged D mesons decays in the signal mode uniformly in phase space, while the other D meson decays in all known modes with relevant branching fractions. These underlying events are input to the CLEO-c detector simulation and processed with the regular reconstruction package. The MC-generated events are required to pass the same selection requirements as data selected in the signal box, as shown in Fig. 1(a). In each event we consider only the signal mode side to prevent nonuniformity of the efficiency due to the resonance substructure of the other side D decay currently implemented in our generic simulation. The efficiency of the $K\pi\pi$ final state selection for the Dalitz plot analysis is estimated to be $(51.11 \pm 0.07)\%$ where the error is only statistical. This number also accounts for a correction factor, 0.984, due to the nonuniform population of the data on the Dalitz plot,

$$f_{\rm corr} = \frac{\bar{\varepsilon}_{\rm Data}}{\bar{\varepsilon}_{\rm MC}} = \frac{\sum_{n=1}^{N}\varepsilon(x_n, y_n)/N}{\int \varepsilon(x, y)dxdy/\int dxdy}, \tag{5}$$

where $\bar{\varepsilon}_{\rm Data}$ and $\bar{\varepsilon}_{\rm MC}$ are the average efficiencies for data and uniformly generated MC samples, the function $\varepsilon(x, y)$ is an efficiency over Dalitz plot defined later by Eqs. (6) and (7), the sum runs over all N events in the data sample, and the integrals are taken over the area of the Dalitz plot.

To parametrize the efficiency $\varepsilon(x, y)$, we use a symmetric third-order polynomial function centered on the arbitrary point $(x_c, y_c) = (1.5, 1.5)$ $(\mathrm{GeV}/c^2)^2$ on the Dalitz plot. With $\hat{x} \equiv x - x_c$ and $\hat{y} \equiv y - y_c$, the efficiency is the product of the polynomial function:

$$\varepsilon(x, y) = T(v)[1 + E_1(\hat{x} + \hat{y}) + E_2(\hat{x}^2 + \hat{y}^2) + E_3(\hat{x}^3 + \hat{y}^3) + E_{xy}\hat{x}\,\hat{y} + E_{xyn}(\hat{x}^2\hat{y} + \hat{x}\hat{y}^2)], \quad (6)$$

and sinelike threshold factors for each Dalitz plot variable v ($\equiv x$, y or z):

$$T(v) = \begin{cases} \sin(E_{\mathrm{th},v}|v - v_{\max}|) & \text{for } 0 < E_{\mathrm{th},v}|v - v_{\max}| < \pi/2, \\ 1 & \text{for } E_{\mathrm{th},v}|v - v_{\max}| \geq \pi/2, \end{cases} \quad (7)$$

where all polynomial coefficients E_1, E_2, E_3, E_{xy}, E_{xyn}, and $E_{\mathrm{th},v}$ are the fit parameters. Each variable v has two thresholds $v_{\min}$ and $v_{\max}$. We expect low efficiency in the regions $v \approx v_{\max}$ only, where one of three particles is produced with zero momentum in the D-meson rest frame and thus has a small momentum in the laboratory frame. Figure 4 and Table I show results of the fit to the entire signal MC sample of $D^+ \to K^-\pi^+\pi^+$ events selected on the Dalitz plot. The polynomial function with threshold factors well describes the efficiency shape. If we consider subsamples of our signal MC, such as D^+ versus D^-, we find that the variation of the efficiency parameters is small compared to their statistical uncertainties. In fits to data we use this efficiency shape with fixed parameters, and variations constrained by the errors from our fit to the signal MC are allowed as systematic checks.

TABLE I. Fit parameters for the efficiency from the signal MC sample.

Parameter	Value
E_1	-0.0153 ± 0.0090
E_2	-0.030 ± 0.011
E_3	0.162 ± 0.020
E_{xy}	-0.053 ± 0.019
E_{xyn}	0.673 ± 0.055
$E_{\mathrm{th},x} \equiv E_{\mathrm{th},y}$	4.25 ± 0.23
$E_{\mathrm{th},z}$	2.907 ± 0.075
Pearson χ^2/ν	649/573
Probability (%)	1.5
Events on DP	477978

E. Background parametrization

A shape for the background on the Dalitz plot is estimated using data events from a $m_{\rm BC}$ sideband region, shown by the hatched box in Fig. 1(a). This box is shifted in ΔE from the signal region to have the same $K^-\pi^+\pi^+$ invariant mass range as candidates in the signal box. We consider only events from the low-mass $m_{\rm BC}$ sideband as the high-mass sideband has a significant contribution from signal events due to a "tail" caused by initial state radiation. This tail is clearly seen in the $m_{\rm BC}$ distribution shown in Fig. 1(b).

The background is a small contribution that has little effect on our fits. Nevertheless, we study the background composition using generic MC simulation for all known modes and find the following. The pileup of events at $m^2(K\pi)_{\rm high} \approx 2.6\ \mathrm{GeV}^2/c^4$ is caused by the misreconstructed D decays from $D^0\bar{D}^0$ and D^+D^- pairs and the combinatorial background from the $e^+e^- \to q\bar{q}$ ($q = u, d$ and s) continuum; their contributions have the relative fractions of 62%, 13% and 25%, respectively, in this

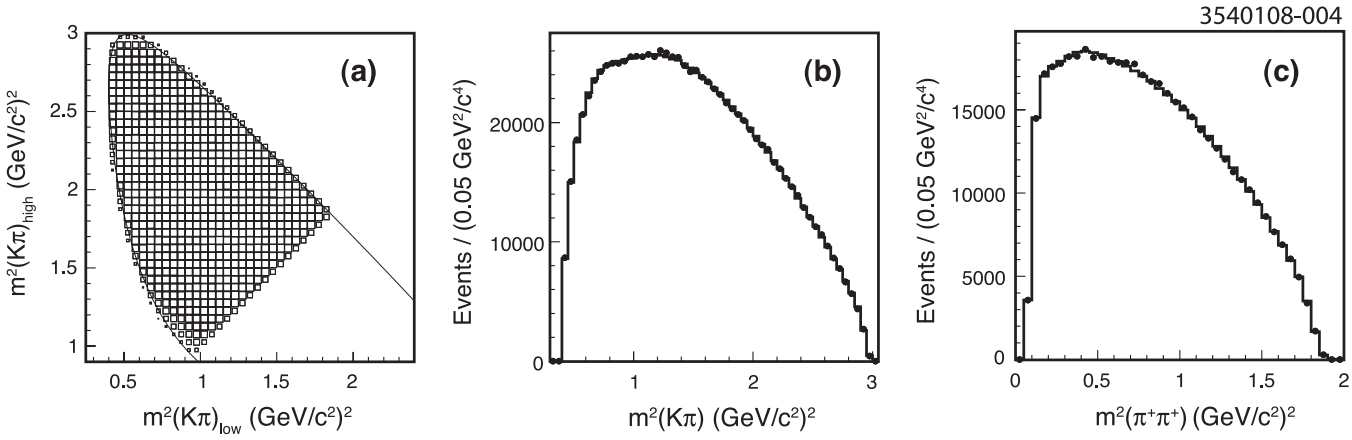

FIG. 4. For the efficiency shape: (a) Dalitz plot of the signal MC generated uniformly in phase space and its projections on (b) $m^2(K\pi)$ (two entries per event) and (c) $m^2(\pi\pi)$ variables. The solid histogram is a projection of the function described in the text which parametrizes the efficiency. Binned results are shown, but the efficiency shape is determined with an unbinned maximum likelihood fit.

3540108-005

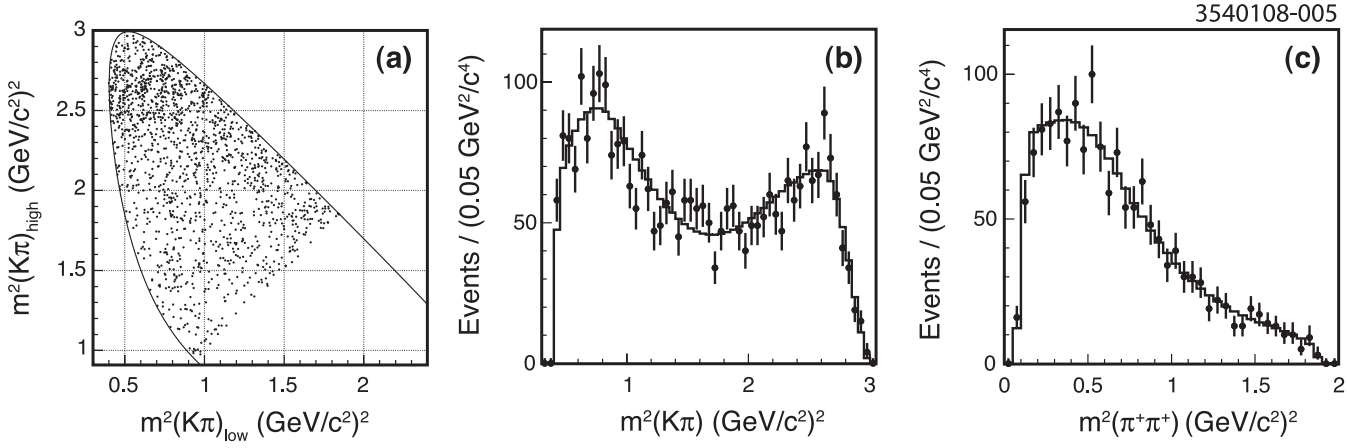

FIG. 5. (a) Dalitz plot of data in the sideband box and projections on (b) $m^2(K\pi)$ (two entries per event) and (c) $m^2(\pi\pi)$ variables. The solid histogram shows the projection of the fit function used to parametrize the background shape described in the text.

TABLE II. Fit parameters for the background shape from the fit to the sideband region.

Parameter	Nominal value
B_1	0.63 ± 0.22
B_2	0.95 ± 0.39
B_3	0.41 ± 0.54
B_{xy}	-0.20 ± 0.62
B_{xyn}	-1.2 ± 1.3
$B_{\mathrm{th},x} \equiv B_{\mathrm{th},y}$	1.31 ± 0.13
$B_{\mathrm{th},z}$	11.2 ± 6.5
Pearson χ^2/ν	129/97
Probability (%)	1.6
Events on DP	1554

area. The dominant misreconstructed D decays are $D^0 \to K^-\pi^+\pi^0$, $a_1(1260)^+K^-$, and $D^+ \to K^-\pi^+\pi^+$, where one of the final state pions is misreconstructed and replaced with a π^+ meson from the other D decay. The shape of the background is well reproduced in our simulation for events selected from either the signal or sideband box.

To parametrize the background shape on the Dalitz plot we employ a function similar to that used for the efficiency, shown in Eqs. (6) and (7). Figure 5 and Table II show results of the fit with the background polynomial function to our sideband sample. In cross-checks with subsamples we find the variation of the shape parameters is small compared to their statistical uncertainties. We use the nominal background shape with fixed parameters in fits to data and allow the parameters to vary constrained by their errors as a systematic check.

III. DECAY AMPLITUDE PARAMETRIZATION

A. Matrix element

In this analysis we follow the formalism of E791 [7] with only minor variations. In the formulas below for the Dalitz plot variables, we also use Mandelstam notations $s = m^2(K^-\pi_1^+)$, $t = m^2(K^-\pi_2^+)$, and $u = m^2(\pi_1^+\pi_2^+)$. We choose two of them s and t as independent, and the third u is dependent, constrained by the equation $s + t + u = m_D^2 + m_K^2 + 2m_\pi^2$. Then, the matrix element has an explicit Bose-symmetric form for pion permutations

$$\mathcal{M}(s,t) = A(s,t) + A(t,s) + A^{I=2}_{L=0}(u(s,t)). \tag{8}$$

Below we discuss the amplitudes contributing to the matrix element.

B. Partial $K\pi$ amplitudes

Each $K\pi$ amplitude is defined using a sum over the decay orbital momentum L of two-body partial waves

$$A(s,t) = \sum_{L=0}^{L_{\max}} \Omega_L(s,t)\mathcal{F}_D^L(q(s))\mathcal{A}_L(s), \tag{9}$$

with parameters as described below. In this analysis we consider the sum up to the maximal orbital momentum $L_{\max} = 2$.

We assume the $D^+ \to K^-\pi^+\pi^+$ decay goes via a quasi-two-body intermediate state $d \to Rc$ containing the resonance R and particle c, followed by the decay of the resonance to the final stable particles a and b, $R \to ab$. This is shown schematically in Fig. 6. The $\Omega_L(s,t)$ term in Eq. (9) represents the angular distribution, which we use in the invariant forms [18]

$$\Omega_{L=0}(m_{ab}^2, m_{ac}^2) = 1, \tag{10}$$

$$\Omega_{L=1}(m_{ab}^2, m_{ac}^2) = m_{bc}^2 - m_{ac}^2 + \frac{(m_d^2 - m_c^2)(m_a^2 - m_b^2)}{m_{ab}^2}, \tag{11}$$

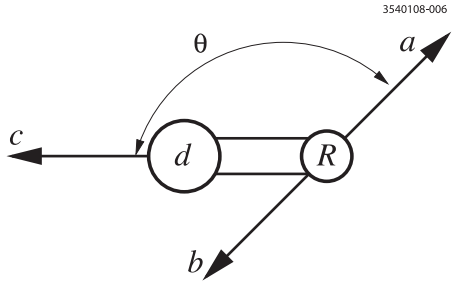

FIG. 6. Three-body decay $d \to Rc \to abc$ in the resonance R rest frame.

$$\Omega_{L=2}(m_{ab}^2, m_{ac}^2) = [\Omega_{L=1}]^2 - \frac{1}{3}\left(m_{ab}^2 - 2m_d^2 - 2m_c^2 + \frac{(m_d^2 - m_c^2)^2}{m_{ab}^2}\right)\left(m_{ab}^2 - 2m_a^2 - 2m_b^2 + \frac{(m_a^2 - m_b^2)^2}{m_{ab}^2}\right), \quad (12)$$

where m_d, m_a, m_b, and m_c are the masses of decaying and product particles and m_{ab}, m_{ac}, and m_{bc} are the relevant invariant masses. In the appendix we show that these angular distributions are equivalent to those applied in the E791 analysis [7] up to constant coefficients.

The form factors $\mathcal{F}_D^L(q)$ in Eq. (9) and $\mathcal{F}_R^L(q)$ in Eqs. (20) and (22) are defined using the Blatt-Weisskopf form [19]

$$L = 0\text{: } \mathcal{F}_V^0(q) = 1, \quad (13)$$

$$L = 1\text{: } \mathcal{F}_V^1(q) = \sqrt{\frac{1 + q_V^2}{1 + q^2}}, \quad (14)$$

$$L = 2\text{: } \mathcal{F}_V^2(q) = \sqrt{\frac{9 + 3q_V^2 + q_V^4}{9 + 3q^2 + q^4}}, \quad (15)$$

where the index V stands for the D or R decay vertex, $q = r_V \mathrm{P}$, P is the magnitude of the momentum of the decay products in the decaying particle's rest frame, and r_V is the effective radius for the D or R vertex, respectively. For both D and R decays, $q_V = r_V \mathrm{P}_V$, where P_V is the magnitude of momentum of the decay products calculated at $m_{ab} = m_R$, the pole mass of R. The form factors are normalized by the condition $\mathcal{F}_V^L(q_V) = 1$.

The values of radial parameters are discussed in Sec. IV. Expressions for the decay products' momentum for both vertices can be found in the appendix. The mass dependences of $\mathcal{F}_D^L(q(s))$ form factors for $K\pi$ resonances are shown in Table III.

Another Gaussian form factor shape of the scalar resonance,

$$\mathcal{F}_V^0(q) = e^{-(q^2 - q_V^2)/12}, \quad (16)$$

is applied in the E791 [7] analysis. This shape is suggested by Tornquist [20] and has a steep dependence on momentum. A reanalysis of the E791 data [10] found that this form factor is not required by the data. We use only the Gaussian form factors $\mathcal{F}_D^0$ and $\mathcal{F}_R^0$ from Eq. (16) for the scalar components κ and $K_0^*(1430)$, when comparing results with E791 model C [6]. We use the unit form factor from Eq. (13) for scalar resonances in all other models and with the binned partial waves discussed below.

The partial waves $\mathcal{A}_L(s)$ in Eq. (9) are the angular momentum L-dependent functions of a single variable z, which is either s or t. In the $D^+ \to K^-\pi^+\pi^+$ decay the S, P and D waves ($L = 0$, 1, or 2, respectively) are represented by the sum of functions W_R for individual intermediate states

$$\mathcal{A}_0(z) = c_{NR} + W_\kappa + W_{K_0^*(1430)} + W_{S,\mathrm{binned}}, \quad (17)$$

$$\mathcal{A}_1(z) = W_{K^*(892)} + W_{K^*(1410)} + W_{K^*(1680)} + W_{P,\mathrm{binned}}, \quad (18)$$

$$\mathcal{A}_2(z) = W_{K_2^*(1430)} + W_{D,\mathrm{binned}}. \quad (19)$$

The contribution of nonresonant decays is represented by $c_{NR} = a_{NR} e^{i\phi_{NR}}$, a complex constant with two fit parameters for magnitude a_{NR} and phase ϕ_{NR}. The $W_{L,\mathrm{binned}}$ are the binned amplitudes as discussed below.

$$W_R = c_R \mathcal{W}_R \mathcal{F}_R^L(r_R \mathrm{P}) \quad (20)$$

is the shape of an individual resonance $\mathcal{W}_R$ [see Eqs. (21)–(24)] multiplied by the form factor in the resonance R decay vertex $\mathcal{F}_R^L(r_R \mathrm{P})$ and the coupling constant $c_R = a_R e^{i\phi_R}$. The resonance R production magnitudes a_R and phases ϕ_R are parameters of the fit to the Dalitz plot.

C. Resonance shapes

For intermediate $K\pi$ resonances we use the standard Breit-Wigner function

$$\mathcal{W}_R(m) = \frac{1}{m_R^2 - m^2 - i m_R \Gamma(m)}, \quad (21)$$

where $m^2 = s$ and the mass-dependent width has the usual form

$$\Gamma(m) = \Gamma_R \frac{m_R}{m}\left(\frac{\mathrm{P}}{\mathrm{P}_R}\right)^{2L+1} [\mathcal{F}_R^L(r_R \mathrm{P})]^2. \quad (22)$$

For $K_0^*(1430)$ we have tested both the Breit-Wigner function [Eq. (21)] and the Flatté parametrization

$$\mathcal{W}_R(m) = \frac{1}{m_R^2 - m^2 - i\sum_{ab} g_{Rab}^2 \rho_{ab}(m)}, \quad (23)$$

where g_{Rab} is a coupling constant of resonance R to the final state ab and $\rho_{ab}(m) = 2\mathrm{P}/m$ is a phase space factor. We test the Flatté parametrization because the $K_0^*(1430)$

TABLE III. Bins for the $K\pi$ S, P, and D waves and Blatt-Weisskopf form factors for $K^*(892)$ and $K^*(1680)$ from Eq. (14), $K_2^*(1430)$ from Eq. (15), and $K_0^*(1430)$ from Eq. (16), calculated in the D-meson decay vertex.

Bin #	$m^2_{K\pi}$ $(\mathrm{GeV}/c^2)^2$ Bin range	$m_{K\pi}$ (GeV/c^2) Bin range	Center	Blatt-W. form factors $\mathcal{F}_D^L(q)$ for $K^*(892)$	$K^*(1680)$	$K_2^*(1430)$	Gaussian FF $K_0^*(1430)$
1	0.4–0.5	0.632–0.707	0.671	0.888	0.250	0.305	0.347
2	0.5–0.6	0.707–0.775	0.742	0.918	0.259	0.324	0.380
3	0.6–0.7	0.775–0.837	0.806	0.948	0.267	0.345	0.415
4	0.7–0.8	0.837–0.894	0.866	0.982	0.277	0.368	0.451
5	0.8–0.9	0.894–0.949	0.922	1.017	0.287	0.394	0.489
6	0.9–1.0	0.949–1.000	0.975	1.055	0.297	0.421	0.528
7	1.0–1.1	1.000–1.049	1.025	1.096	0.309	0.452	0.570
8	1.1–1.2	1.049–1.095	1.072	1.140	0.321	0.485	0.612
9	1.2–1.3	1.095–1.140	1.118	1.188	0.335	0.523	0.656
10	1.3–1.4	1.140–1.183	1.162	1.240	0.349	0.564	0.700
11	1.4–1.5	1.183–1.225	1.204	1.296	0.365	0.609	0.746
12	1.5–1.6	1.225–1.265	1.245	1.358	0.383	0.659	0.792
13	1.6–1.7	1.265–1.304	1.285	1.425	0.402	0.715	0.839
14	1.7–1.8	1.304–1.342	1.323	1.499	0.423	0.776	0.885
15	1.8–1.9	1.342–1.378	1.360	1.581	0.446	0.844	0.932
16	1.9–2.0	1.378–1.414	1.396	1.672	0.471	0.918	0.978
17	2.0–2.1	1.414–1.449	1.432	1.773	0.500	0.999	1.023
18	2.1–2.2	1.449–1.483	1.466	1.886	0.532	1.085	1.067
19	2.2–2.3	1.483–1.517	1.500	2.013	0.568	1.178	1.109
20	2.3–2.4	1.517–1.549	1.533	2.157	0.608	1.275	1.150
21	2.4–2.5	1.549–1.581	1.565	2.320	0.654	1.374	1.189
22	2.5–2.6	1.581–1.612	1.597	2.506	0.707	1.472	1.226
23	2.6–2.7	1.612–1.643	1.628	2.719	0.766	1.568	1.259
24	2.7–2.8	1.643–1.673	1.658	2.962	0.835	1.657	1.290
25	2.8–2.9	1.673–1.703	1.688	3.240	0.913	1.737	1.318
26	2.9–3.0	1.703–1.732	1.718	3.554	1.002	1.805	1.342
$m_{K\pi,\mathrm{min}} = m_{K^-} + m_{\pi^+} = 0.633\ \mathrm{GeV}/c^2$							
$m_{K\pi,\mathrm{max}} = m_{D^+} - m_{\pi^+} = 1.730\ \mathrm{GeV}/c^2$							

mass is close to the $K\eta$ and $K\eta'$ thresholds, which could significantly distort the resonance shape [10].

For a low invariant mass $K\pi$ S wave we tested the Breit-Wigner function, following E791, and the complex pole proposed in Ref. [11]

$$\mathcal{W}_R(m) = \frac{1}{s_R - m^2}, \tag{24}$$

where s_R is a pole position in the complex $s = m^2$ plane. This function represents the first term of the Laurent series in the expansion of the chiral perturbation theory complex amplitude for the scalar wave. This approach is common, and a survey of pole positions extracted from different experiments can also be found in Ref. [9]. This complex pole is equivalent to a Breit-Wigner function with constant width.

D. Isospin-two $\pi^+\pi^+$ S wave amplitude

The isospin-two $\pi^+\pi^+$ S wave amplitude in Eq. (8) is a sum of two components

$$A^{I=2}_{L=0}(u) = c_{\pi\pi}\mathcal{W}^{I=2}_S + W^{I=2}_{S,\mathrm{binned}}, \tag{25}$$

where $c_{\pi\pi} = a_{\pi\pi}e^{i\phi_{\pi\pi}}$ is a complex coupling constant and $W^{I=2}_{S,\mathrm{binned}}$ is discussed in Sec. III E. The first term of this sum is parametrized by a unitary form [21]

$$\mathcal{W}^{I=2}_S(m) = \frac{\eta_0^2(m)e^{2i\delta_0^2(m)} - 1}{2i}, \tag{26}$$

where m is a $\pi^+\pi^+$ invariant mass, $\eta_0^2(m)$ is an inelasticity, and $\delta_0^2(m)$ is a phase of the $\pi^+\pi^+$ wave with total spin 0 and isospin two. The phase $\delta_0^2(m)$ is assumed to be proportional to the decay momentum at threshold and sculpted by a polynomial function at higher mass range

$$\delta_0^2(m) = \frac{-a\sqrt{m^2/4 - m_\pi^2}}{1 + bm^2 + cm^4 + dm^6}, \tag{27}$$

with parameters $a = (55.21 \pm 3.18)$ deg/GeV, $b = (0.853 \pm 0.254)\ \mathrm{GeV}^{-2}$, $c = (-0.959 \pm 0.247)\ \mathrm{GeV}^{-4}$, and $d = (0.314 \pm 0.070)\ \mathrm{GeV}^{-6}$, obtained in Ref. [21] from a fit to the data of the scattering experiments [12]. We use this function with fixed parameters. The inelasticity $\eta_0^2(m)$ in the mass range of $m < m_{\mathrm{min}} \approx m(\rho^+\rho^+) \approx 1.5\ \mathrm{GeV}/c^2$ is expected to be near unity. Then $\eta_0^2(m)$

TABLE IV. The Breit-Wigner resonance parameters used or measured in the isobar model; CLEO-c vs E791. The fixed parameters used in the E791 experiment are taken from PDG 2000 [22] with their uncertainties shown in square brackets. The measured values are shown with two uncertainties: statistical and systematic. The values shown in parentheses (with statistical error only) were obtained in cross-checks when these parameters are allowed to float.

Parameter (MeV/c^2)	E791 [PDG 2000]	CLEO-c		PDG 2006 [1]
		Model C (if float)	Model I2 (if float)	
$m_{K^*(892)}$	896.1[$\pm$0.27]	896(894.8 $\pm$ 0.5)	895.7 $\pm$ 0.2 $\pm$ 0.3	896.00 $\pm$ 0.25
$\Gamma_{K^*(892)}$	50.7[$\pm$0.6]	50.3(45.5 $\pm$ 0.4)	45.3 $\pm$ 0.5 $\pm$ 0.6	50.3 $\pm$ 0.6
$m_{K^*(1430)}$	1459 $\pm$ 7 $\pm$ 12	1463.0 $\pm$ 0.7 $\pm$ 2.4	1466.6 $\pm$ 0.7 $\pm$ 3.4	1414 $\pm$ 6
$\Gamma_{K^*(1430)}$	175 $\pm$ 12 $\pm$ 12	163.8 $\pm$ 2.7 $\pm$ 3.1	174.2 $\pm$ 1.9 $\pm$ 3.2	290 $\pm$ 21
$m_{K_2^*(1430)}$	1432.4[$\pm$1.3]	1432.4(1436 $\pm$ 11)	1432.4(1427 $\pm$ 7)	1432.4 $\pm$ 1.3
$\Gamma_{K_2^*(1430)}$	109[$\pm$5]	109(132 $\pm$ 21)	109(120 $\pm$ 13)	109 $\pm$ 5
$m_{K^*(1680)}$	1717[$\pm$27]	1717(1782 $\pm$ 41)	1717(1679 $\pm$ 59)	1717 $\pm$ 27
$\Gamma_{K^*(1680)}$	322[$\pm$110]	322(565 $\pm$ 131)	322(446 $\pm$ 119)	322 $\pm$ 110
$m_{K^*(1410)}$	1414[$\pm$15]	1414	1414	1414 $\pm$ 15
$\Gamma_{K^*(1410)}$	232[$\pm$21]	232	232	232 $\pm$ 21
m_κ	797 $\pm$ 19 $\pm$ 43	809 $\pm$ 1 $\pm$ 13	Complex pole,	$K_0^*(800)$ is not
Γ_κ	410 $\pm$ 43 $\pm$ 87	470 $\pm$ 9 $\pm$ 15	see Table VI	established

decreases due to the $\pi^+\pi^+ \to \rho^+\rho^+$ rescattering at a higher mass range. In our fits we use a smooth approximation for this threshold behavior

$$\eta_0^2(m) = \begin{cases} 1, & m \le m_{\min}, \\ 1 - \frac{\Delta\eta}{2}[1 - \cos(\pi \frac{m - m_{\min}}{m_{\max} - m_{\min}})], & m_{\min} < m < m_{\max}, \\ 1 - \Delta\eta, & m \ge m_{\max}, \end{cases} \tag{28}$$

with fit parameters $m_{\min}$, $m_{\max}$, and $\Delta\eta$.

E. Binned amplitude

The complex term $W_{L,\text{binned}}$ in Eqs. (17)–(19) and (25), where $L = 0$, 1, or 2, is intended to provide a completely model-free parametrization of the partial wave. It can be used alone or in combination with other terms. In the latter case it represents a correction to the complex amplitude of the isobar model. We use this term in the form of an s-dependent complex number

$$W_{L,\text{binned}}(s) = a_L(s)e^{i\phi_L(s)}, \tag{29}$$

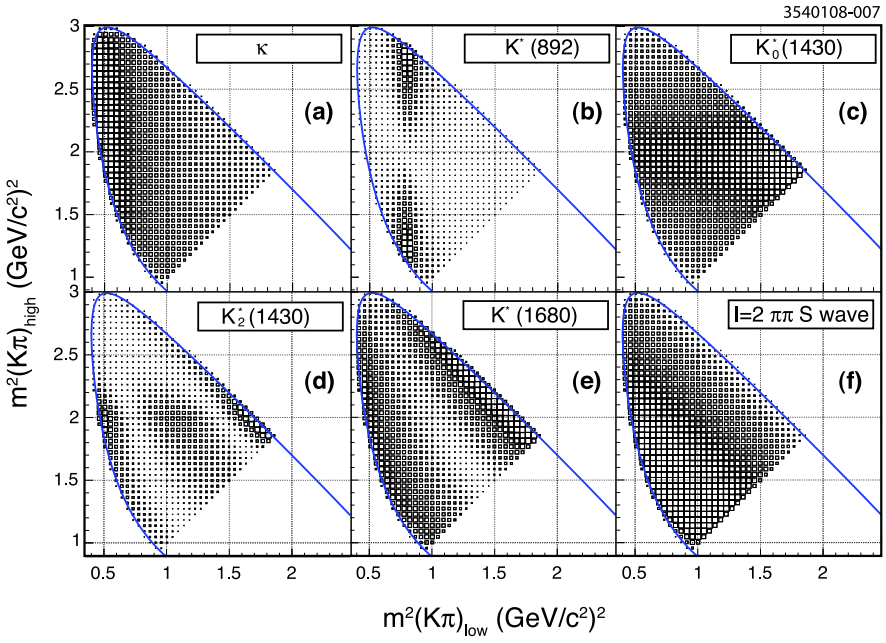

FIG. 7 (color online). Simulation of the expected contribution to the $D^+ \to K^-\pi^+\pi^+$ Dalitz plot from various intermediate states. (a) Low-mass $K\pi$ S wave (κ), (b) $K^*(892)\pi$, (c) $K_0^*(1430)\pi$, (d) $K_2^*(1430)\pi$, (e) $K^*(1680)\pi$, and (f) $K(\pi\pi)_{I=2}$ with $I = 2$ $\pi^+\pi^+$ S wave.

with functions $a_L(s)$ and $\phi_L(s)$ defined by an interpolation between the bins for the magnitude a_{Lk} and phase ϕ_{Lk}, where $k(s) = 1, 2, \ldots, N_L$ is an s-dependent index of these bins. For all $K\pi$ waves we define $N_L = 26$ uniform bins in $s \equiv m^2_{K\pi}$ in the range $[0.4, 3.0]$ $(\mathrm{GeV}/c^2)^2$, as shown in Table III. Similar, for an $I = 2$ $\pi^+\pi^+$ S wave we define $N^{I=2}_{L=0} = 18$ uniform bins in $u \equiv m^2_{\pi\pi}$ [s in Eq. (29) is replaced with u] in the range $[0.1, 1.9]$ $(\mathrm{GeV}/c^2)^2$. This binning scheme covers the kinematically allowed range of the $K\pi$ $[0.633, 1.730]$ GeV/c^2 and $\pi^+\pi^+$ $[0.279, 1.376]$ GeV/c^2 invariant mass spectrum in the $D^+ \to K^-\pi^+\pi^+$ decay. We interpolate linearly between bin centers in our fitting function.

F. Fit fraction

We estimate a contribution of each component in the matrix element using a standard definition of the fit fraction

$$\mathrm{FF}_R = \frac{\int |A_R(x, y)|^2 dxdy}{\int |M(x, y)|^2 dxdy}, \tag{30}$$

where $A_R(x, y)$ is an amplitude contribution from the R component to the total matrix element $M(x, y)$ from Eq. (8) and the integrals are taken over the area of the Dalitz plot.

G. Expected contributions

A priori, all known $K\pi$ resonances in the mass range from the production threshold up to 1.73 GeV/c^2, such as $K^*(892)$, $K^*(1410)$, $K^*_0(1430)$, $K^*_2(1430)$, $K^*(1680)$, and even higher mass resonances, might contribute to the amplitude of the $D^+ \to K^-\pi^+\pi^+$ decay. Table IV shows parameters of $K\pi$ resonances which have been considered in this analysis. One would also foresee an $I = 2$ $\pi^+\pi^+$ S wave final state interaction. Simulations of some of the expected contributions to the Dalitz plot are shown in Fig. 7. In contrast to the data [Fig. 2(a)], the $K^*(892)$ population density in Fig. 7(b) is symmetric without interference with an S wave.

IV. FITS TO DATA USING THE ISOBAR MODEL

A. Comparison with E791 model C

First we compare our results, obtained in the framework of the isobar model, with E791 models A, B, and C from Ref. [6]. In particular, the most complete model C contains $\bar{K}^*(892)\pi^+$, $\bar{K}^*_0(1430)\pi^+$, $\bar{K}^*_2(1430)\pi^+$, $\bar{K}^*(1680)\pi^+$, $\kappa\pi^+$, and nonresonant (NR) contributions. Following E791 we allow a scalar $K\pi$ amplitude, the "κ," as a Breit-Wigner resonance with mass-dependent width. We set $c_{K^*(892)} = 1$ in Eqs. (18) and (20), and all other magnitudes and phases are defined with respect to $K^*(892)$. Gaussian form factors $\mathcal{F}^0_D(r_D \mathrm{P}_c)$ and $\mathcal{F}^0_R(r_R \mathrm{P})$ from Eq. (16) are used for $K^*_0(1430)$ and κ. For all $K\pi$ resonances with nonzero spin, the radii in the Blatt-Weisskopf [19] form factors $r_D = 5$ GeV^{-1} and $r_R = 1.5$ GeV^{-1} are fixed to the values used by E791. On the Dalitz plot, the p.d.f. for this model looks indistinguishable from statistics shown in Fig. 2(a). The Dalitz plot projections with p.d.f. components are shown in Fig. 8. Fit fractions and phases, obtained in our fit, are compared with E791 [6] in Table V and are statistically consistent. Magnitudes are not comparable because of a different choice for normalization. The values obtained for resonance parameters are compared in Table IV. In particular, we get dominant contributions from S wave components; the NR, $K^*_0(1430)\pi$, and $\kappa\pi$ fit fractions are $\approx 9\%$, 10%, and 33%, respectively. The total sum of all fit fractions is 65.5%, indicating substantial constructive interference. Apparently, model C gives a poor fit quality $\chi^2/\nu = 531/391$. A large discrepancy between the fit and the data is seen in Fig. 8 for the $m^2(\pi^+\pi^+)$ projection in the range of $[1.4, 1.9]$ $(\mathrm{GeV}/c^2)^2$. That motivates us to explore alternative models of the decay amplitude.

B. Variations of model C

The Gaussian form factors, given by Eq. (16) for scalar resonances $\mathcal{F}^0_R(r_R \mathrm{P})$ and $\mathcal{F}^0_D(r_D \mathrm{P}_c)$, behave similarly to the $L = 4$ Blatt-Weisskopf form factor. This behavior is not preferred by either our or the E791 data; see Ref. [10] for details. With our data we find that results are not very dependent on the assumed resonance decay vertex form factor $\mathcal{F}^0_R(r_R \mathrm{P})$. However, the D-meson decay vertex form factor $\mathcal{F}^0_D(r_D \mathrm{P})$ changes the S wave dependence on s significantly. In particular, this Gaussian form factor (see Table III) suppresses the contribution of $K\pi$ at low mass. To agree with the data when fitting with this factorized form factor, the magnitude of the complex function (S wave) increases at low $K\pi$ mass which gives an illusion of resonance behavior. For all models other than model C below we use unit form factors from Eq. (13) for S wave contributions.

For the $K^*_0(1430)$ resonance we measure $m_{K^*_0(1430)} = 1463.0 \pm 0.7 \pm 2.4$ MeV/c^2 and $\Gamma_{K^*_0(1430)} = 163.8 \pm 2.7 \pm 3.1$ MeV/c^2, which are consistent with E791 results but inconsistent with current PDG [1] values, as demonstrated in Table IV. Similar behavior is reported in Ref. [23] from the FOCUS Collaboration. In Ref. [10] Bugg surmises that the $K^*_0(1430)$ resonance parameters might change due to the opening of the $K\eta'$ channel. In order to accommodate this effect, we test the Flatté parametrization of Eq. (23), which depends on a floating mass $m_{K^*_0(1430)}$ and three coupling constants $g_{K\pi}$, $g_{K\eta}$, and $g_{K\eta'}$. We find that our data are consistent with $g_{K\eta} = 0$, and this coupling is dropped from further consideration. The resulting values of the other parameters are shown in Table VI. We do not find any significant difference between Breit-Wigner and Flatté parametrizations in the shape of the $K^*_0(1430)$ complex amplitude or in the fit quality.

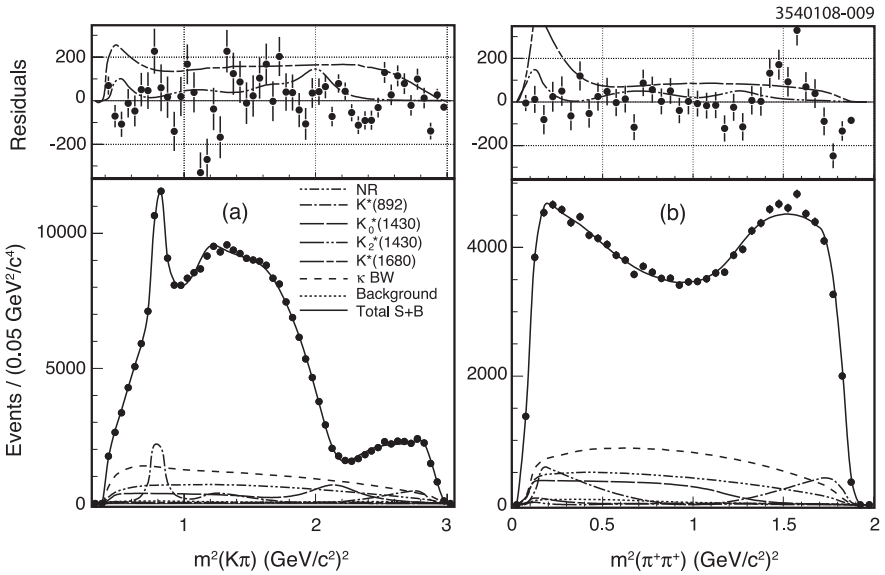

FIG. 8. Projections of the fit to the Dalitz plot with model C on (a) $m^2(K\pi)$ (two entries per event) and (b) $m^2(\pi\pi)$ variables. Residuals between data and the total p.d.f. are shown by dots with statistical error bars on the top insets along with minor contributions from the $K^*(1680)$ and $K_2^*(1430)$ resonances, plotted with factor $\times 4$.

TABLE V. Comparison of CLEO-c results with E791 using the isobar fit, model C. Shown are the fitted magnitudes, a in arbitrary units, the phases, ϕ in degrees, defined relative to the $K^*(892)\pi^+$ amplitude, and the FF. Also indicated are the fitted masses m and widths Γ of the spin-zero resonances. Magnitudes a are not comparable between the two experiments because of a different choice for normalization.

Mode	Parameter	E791	CLEO-c
NR	a	$1.03 \pm 0.30 \pm 0.16$	$7.4 \pm 0.1 \pm 0.6$
	$\phi(^\circ)$	$-11 \pm 14 \pm 8$	$-18.4 \pm 0.5 \pm 8.0$
	FF (%)	$13.0 \pm 5.8 \pm 4.4$	$8.9 \pm 0.3 \pm 1.4$
$\bar{K}^*(892)\pi^+$	a	1 (fixed)	1 (fixed)
	$\phi(^\circ)$	0 (fixed)	0 (fixed)
	FF (%)	$12.3 \pm 1.0 \pm 0.9$	$11.2 \pm 0.2 \pm 2.0$
$\bar{K}_0^*(1430)\pi^+$	a	$1.01 \pm 0.10 \pm 0.08$	$3.00 \pm 0.06 \pm 0.14$
	$\phi(^\circ)$	$48 \pm 7 \pm 10$	$49.7 \pm 0.5 \pm 2.9$
	FF (%)	$12.5 \pm 1.4 \pm 0.5$	$10.4 \pm 0.6 \pm 0.5$
	m (MeV/c^2)	$1459 \pm 7 \pm 12$	$1463.0 \pm 0.7 \pm 2.4$
	Γ (MeV/c^2)	$175 \pm 12 \pm 12$	$163.8 \pm 2.7 \pm 3.1$
$\bar{K}_2^*(1430)\pi^+$	a	$0.20 \pm 0.05 \pm 0.04$	$0.962 \pm 0.026 \pm 0.050$
	$\phi(^\circ)$	$-54 \pm 8 \pm 7$	$-29.9 \pm 2.5 \pm 2.8$
	FF (%)	$0.5 \pm 0.1 \pm 0.2$	$0.38 \pm 0.02 \pm 0.03$
$\bar{K}^*(1680)\pi^+$	a	$0.45 \pm 0.16 \pm 0.02$	$6.5 \pm 0.1 \pm 1.5$
	$\phi(^\circ)$	$28 \pm 13 \pm 15$	$29.0 \pm 0.7 \pm 4.6$
	FF (%)	$2.5 \pm 0.7 \pm 0.3$	$1.28 \pm 0.04 \pm 0.28$
$\kappa\pi^+$	a	$1.97 \pm 0.35 \pm 0.11$	$5.01 \pm 0.04 \pm 0.27$
	$\phi(^\circ)$	$-173 \pm 8 \pm 18$	$-163.7 \pm 0.4 \pm 5.8$
	FF (%)	$47.8 \pm 12.1 \pm 5.3$	$33.2 \pm 0.4 \pm 2.4$
	m (MeV/c^2)	$797 \pm 19 \pm 43$	$809 \pm 1 \pm 13$
	Γ (MeV/c^2)	$410 \pm 43 \pm 87$	$470 \pm 9 \pm 15$
Form factor	r_κ (GeV^{-1})	1.6 ± 1.3	1.5 (fixed)
	r_D (GeV^{-1})	5.0 ± 0.5	5 (fixed)
Other $R \to K\pi$	r_R (GeV^{-1})	1.5 (fixed)	1.5 (fixed)
$\sum$ FF (%)		88.6	65.5
Goodness	χ^2/ν	46/63	531/391

TABLE VI. Alternative parameters obtained in the fits with the isobar model.

Mode	Amplitude	Parameter (MeV/c^2)	Model C	Model I2
$\bar{K}_0^*(1430)\pi^+$	Breit-Wigner	$m_{K_0^*(1430)}$	$1463.0 \pm 0.7 \pm 2.4$	$1466.6 \pm 0.7 \pm 3.4$
		$\Gamma_{K_0^*(1430)}$	$163.8 \pm 2.7 \pm 3.1$	$174.2 \pm 1.9 \pm 3.2$
	Flatté	$m_{K_0^*(1430)}$	1462.5 ± 3.9	1471.2 ± 0.8
		$g_{K\pi}$	532.9 ± 8.5	546.8 ± 4.2
		$g_{K\eta}$	0	0
		$g_{K\eta'}$	197 ± 106	230 ± 32
$\kappa\pi^+$	Breit-Wigner	m_κ	$809 \pm 1 \pm 13$	888 ± 2
		Γ_κ	$470 \pm 9 \pm 15$	550 ± 12
	Complex pole	$\Re m_\kappa$	769.9 ± 6.3	$706.0 \pm 1.8 \pm 22.8$
		$\Im m_\kappa$	-221.2 ± 8.4	$-319.4 \pm 2.2 \pm 20.2$

TABLE VII. Fit results for model I2, with a Breit-Wigner function or with a complex pole for the κ, and QMIPWA. The FF are shown for a single $K\pi$ wave and need to be doubled as indicated by the "2×" symbol in row titles.

Mode	Parameter	Model I2 (B-W for κ)	Model I2	QMIPWA
$\bar{K}^*(892)\pi^+$	a	1-fixed	1-fixed	1-fixed
	$\phi(^\circ)$	0-fixed	0-fixed	0-fixed
	FF (%) 2×	5.15 ± 0.24	$5.27 \pm 0.08 \pm 0.15$	4.94 ± 0.23
	m (MeV/c^2)	895.4 ± 0.2	$895.7 \pm 0.2 \pm 0.3$	895.7-fixed
	Γ (MeV/c^2)	44.5 ± 0.7	$45.3 \pm 0.5 \pm 0.6$	45.3-fixed
$\bar{K}^*(1680)\pi^+$	a	4.45 ± 0.23	$3.38 \pm 0.16 \pm 0.78$	2.88 ± 0.84
	$\phi(^\circ)$	43.3 ± 3.6	$68.2 \pm 1.6 \pm 13$	113 ± 14
	FF (%) 2×	0.238 ± 0.024	$0.144 \pm 0.013 \pm 0.12$	0.098 ± 0.059
$\bar{K}_2^*(1430)\pi^+$	a	0.866 ± 0.030	$0.915 \pm 0.025 \pm 0.04$	0.794 ± 0.073
	$\phi(^\circ)$	-17.4 ± 3.5	$-17.4 \pm 2.3 \pm 2.0$	14.8 ± 9.0
	FF (%) 2×	0.124 ± 0.011	$0.145 \pm 0.009 \pm 0.03$	0.102 ± 0.020
$\bar{K}_0^*(1430)\pi^+$	a	3.97 ± 0.15	$3.74 \pm 0.02 \pm 0.06$	3.74-fixed
	$\phi(^\circ)$	45.1 ± 0.9	$51.1 \pm 0.3 \pm 1.6$	51.1-fixed
	FF (%) 2×	7.53 ± 0.65	$7.05 \pm 0.14 \pm 0.55$	6.65 ± 0.31
	m (MeV/c^2)	1461.1 ± 1.0	$1466.6 \pm 0.7 \pm 3.4$	1466.6-fixed
	Γ (MeV/c^2)	177.9 ± 3.1	$174.2 \pm 1.9 \pm 3.2$	174.2-fixed
$\kappa\pi^+$	a	5.69 ± 0.17	$10.80 \pm 0.05 \pm 0.35$	0
	$\phi(^\circ)$	-149.9 ± 1.2	$148.4 \pm 0.3 \pm 1.6$	0
	FF (%) 2×	8.5 ± 0.5	$21.6 \pm 0.3 \pm 3.2$	0
Pole	$\Re m_0$ (MeV/c^2)		$706.0 \pm 1.8 \pm 22.8$	
	$\Im m_0$ (MeV/c^2)		$-319.4 \pm 2.2 \pm 20.2$	
Breit-Wigner	m (MeV/c^2)	888.0 ± 1.9		
	Γ (MeV/c^2)	550.4 ± 11.8		
NR	a	17.1 ± 0.4	$23.3 \pm 0.1 \pm 1.6$	0
	$\phi(^\circ)$	1.9 ± 1.7	$29.7 \pm 0.2 \pm 3.0$	0
	FF (%)	38.0 ± 1.9	$73.8 \pm 0.8 \pm 9.6$	0
Binned $K^-\pi^+$ S wave	a	0	0	See
	$\phi(^\circ)$	0	0	Table VIII
	FF (%) 2×	0	0	41.9 ± 1.9
$I = 2$ $\pi^+\pi^+$ S wave	a	30.3 ± 2.7	$25.5 \pm 0.3 \pm 2.9$	33.1 ± 2.6
	$\phi(^\circ)$	86.3 ± 3.3	$75.4 \pm 0.6 \pm 10$	66.2 ± 3.5
	FF (%)	13.4 ± 2.3	$9.8 \pm 0.2 \pm 2.0$	15.5 ± 2.8
Equation (28)	$\Delta\eta$	1	1	1
	$m_{\min}$ (MeV/c^2)	1265 ± 8	$1256 \pm 5 \pm 4$	1256.3-fixed
	$m_{\max}$ (MeV/c^2)	1529 ± 31	$1498 \pm 13 \pm 30$	1498.2-fixed
Form factor	r_D (GeV^{-1})	5-fixed	5-fixed	5-fixed
	r_{Swave} (GeV^{-1})	0-fixed	0-fixed	0-fixed
Other $R \to K\pi$	r_R (GeV^{-1})	1.5-fixed	1.5-fixed	1.5-fixed
	$\sum \text{FF}_i$(%)	94.4	152.0	122.8
Goodness	χ^2/ν	426/385	416/385	359/347
	Probability (%)	7.4%	13.2%	31.5%

In model C we also measure the κ resonance Breit-Wigner parameters $m_\kappa = 809 \pm 1 \pm 13$ MeV$/c^2$ and $\Gamma_\kappa = 470 \pm 9 \pm 15$ MeV$/c^2$. In Ref. [11] Oller emphasizes that the Breit-Wigner resonance with a mass-dependent width is not the best choice for the $K\pi$ low-mass phase parametrization. Following his prescription, we replace the Breit-Wigner function by the complex pole from Eq. (24) with the initial pole position at $s_\kappa = (710 - i310)^2$ MeV$^2/c^4$. We allow the pole position to float and obtain its optimal location, as shown in Table VI.

We also test the $K^*(892)$ parameters, as shown in Table IV. The $K^*(892)$ mass is consistent with the PDG [1] value, while the width is about 5 MeV$/c^2$ smaller. In further analysis we allow the $K^*(892)$ mass and width to float.

Inclusion of a $K^*(1410)$ component in the fit does not result in any significant contribution.

C. Model I2

Tuning of the isobar model for $K\pi$ waves only does not improve significantly the probability of consistency between the data and the model, which is still small. The large discrepancy in the $m^2(\pi^+\pi^+)$ spectrum persists even if we use the model-independent parametrization for the $K\pi$ S wave considered below. We solve this problem by including in the matrix element [Eq. (8)] a contribution from the $I = 2$ $\pi^+\pi^+$ S wave, using Eq. (26), which leads to a model called model I2. The threshold of the $\pi^+\pi^+ \to \rho^+\rho^+$ rescattering process is located at the upper edge of the $m^2(\pi^+\pi^+)$ kinematic limit in our decay. The edge of the kinematic border does not allow us to resolve correlations between the $\Delta\eta$ and $m_{\max}$ parameters in Eq. (28). We fix the value of $\Delta\eta = 1$, while floating the $m_{\min}$ and $m_{\max}$ parameters. In model I2, compared to model C, the unit form factors $\mathcal{F}_D^0 = \mathcal{F}_R^0 = 1$ are used for the scalar components, the complex pole amplitude from Eq. (24) is used for the low-mass $K\pi$ S wave, and the $K^*(892)$ parameters are allowed to vary in the fit; other conditions stay the same as in model C.

Model I2 gives the best analytical description of our data. The obtained fit parameters are presented in Table VII. The total p.d.f. and separate components are shown in the Dalitz plot projections in Fig. 9. The large discrepancy in the $m^2(\pi^+\pi^+)$ spectrum is eliminated, improving the probability of consistency between the model and data to 13%.

D. Variations of model I2

We did not find any significant contribution from $K^*(1410)$ by including it in the fit. This resonance is excluded from further consideration.

We also test the alternative descriptions for the $K_0^*(1430)$ parameters as shown Table VI. We do not find any significant difference between Breit-Wigner and Flatté parametrizations in the shape of the $K_0^*(1430)$ complex amplitude or in the fit quality. We therefore use the Breit-Wigner function in model I2 with the mass and width of $K_0^*(1430)$ allowed to float.

The test of alternative descriptions for the low-mass $K\pi$ S wave is presented in Tables VI and VII. The pole amplitude slightly improves the fit quality ($\Delta\chi^2 = -10$) compared to the Breit-Wigner resonance with mass-dependent width. This substitution leads to a significant redistribution of the NR and κ components of the scalar

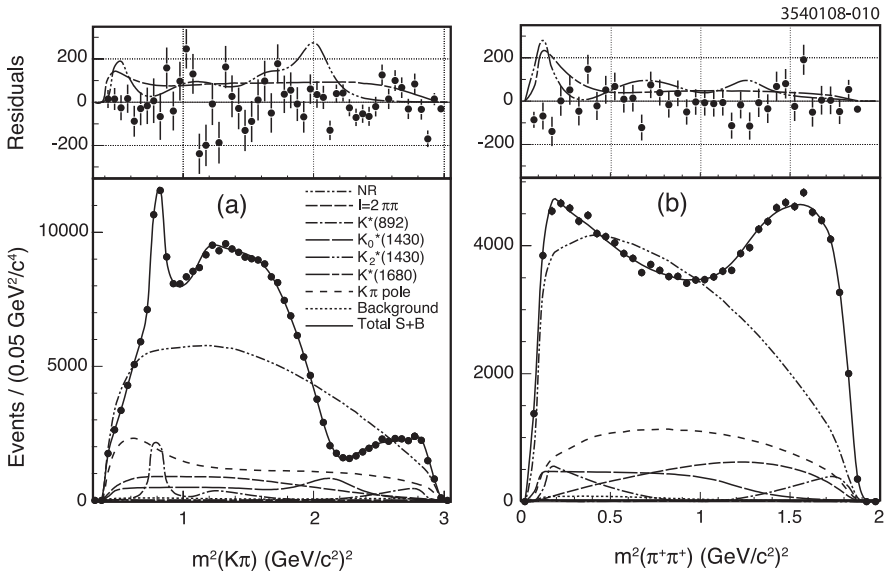

FIG. 9. Projections of the fit to the Dalitz plot with model I2 on (a) $m^2(K\pi)$ (two entries per event) and (b) $m^2(\pi\pi)$ variables. Residuals between data and the total p.d.f. are shown by dots with statistical error bars on the top insets along with minor contributions from the $K^*(1680)$ and $K_2^*(1430)$ resonances, plotted with factor $\times 10$.

wave, though their sum results in very small variation of the complex function. In model I2 we use the pole amplitude for the $K\pi$ low-mass S wave.

V. QUASI-MODEL-INDEPENDENT PARTIAL WAVE ANALYSIS

A. QMIPWA for $K\pi$ S wave

The biggest issue of any Dalitz plot analysis is its model dependence. An attempt to mitigate the model dependence for the decay under study is described in [7]. Here we reproduce this analysis using a slightly modified technique, which we call the quasi-model-independent partial wave analysis (QMIPWA). We apply this technique as an extension of our model I2.

In QMIPWA we modify the parameters of model I2 as follows. The NR and $\kappa\pi$ components in model I2 are replaced by the binned S wave amplitude [Eq. (29)]. The 26 binned S wave magnitudes and phases of $m^2_{K\pi}$ are floating fit parameters. We keep the $K^*_0(1430)\pi$ contribution in its Breit-Wigner form, because it has a sharp structure, that cannot be well reproduced by a binned amplitude. The $K^*_0(1430)$ parameters are fixed to their values from model I2 in order to remove correlations between the Breit-Wigner function and the binned S wave amplitude. The $K\pi$ P wave in Eq. (18) is represented by the $K^*(892)$ and $K^*(1680)$ Breit-Wigner functions, where the $c_{K^*(1680)}$ parameters are allowed to float in the fit. As usual $c_{K^*(892)} = 1$, and all other magnitudes and phases are defined with respect to $K^*(892)$. The $K^*(1410)$ is excluded as mentioned previously. The $K\pi$ D wave in Eq. (19) is represented by the $K^*_2(1430)$ Breit-Wigner function with its parameters $c_{K^*_2(1430)}$ allowed to float in the fit. The $I = 2$ $\pi^+\pi^+$ S wave is represented by the unitary amplitude from Eq. (26) fixing the $m_{\min}$ and $m_{\max}$ parameters to their optimal values from model I2. The $a_{\pi\pi}$ and $\phi_{\pi\pi}$ parameters are allowed to float in the fit.

The results of the QMIPWA fit are shown in Table VII for resonance parameters and Table VIII for the $K\pi$ S wave. Figure 10 shows the Dalitz plot projections of this fit. The measured $K\pi$ S wave and their comparison with model I2 components are displayed in Fig. 11. Both the magnitude and phase are different from those of model I2.

Table VIII (right-hand side) also shows the result of a similar fit for a total binned S wave. For this fit the $K^*_0(1430)$ resonance is accounted for in the binned S wave, and all other parameters are fixed to their values from the nominal QMIPWA fit.

TABLE VIII. QMIPWA: Results for $K\pi$ S wave. Figure 11 shows the binned $K\pi$ S wave without $K^*_0(1430)$ by the dots with error bars and the total $K\pi$ S wave by the solid curve.

Bin #	$m^2_{K\pi}$ $(\mathrm{GeV}/c^2)^2$ Bin range	Binned $K\pi$ S wave w/o $K^*_0(1430)$		Total $K\pi$ S wave	
		Magnitude (a.u.)	Phase (°)	Magnitude (a.u.)	Phase (°)
1	0.4–0.5	$20.23 \pm 0.80 \pm 0.51$	$-71.8 \pm 4.9 \pm 4.1$	19.29 ± 0.56	-66.0 ± 3.2
2	0.5–0.6	$20.90 \pm 0.68 \pm 0.54$	$-61.1 \pm 4.6 \pm 2.3$	20.38 ± 0.51	-54.3 ± 2.8
3	0.6–0.7	$20.58 \pm 0.63 \pm 0.69$	$-48.8 \pm 4.0 \pm 3.2$	20.35 ± 0.45	-40.9 ± 2.2
4	0.7–0.8	$20.62 \pm 0.64 \pm 0.51$	$-47.0 \pm 2.4 \pm 0.7$	20.52 ± 0.59	-39.7 ± 0.9
5	0.8–0.9	$20.95 \pm 0.74 \pm 1.32$	$-44.1 \pm 3.6 \pm 3.5$	20.84 ± 0.49	-36.0 ± 1.4
6	0.9–1.0	$19.97 \pm 0.63 \pm 1.14$	$-38.4 \pm 4.0 \pm 6.4$	19.97 ± 0.36	-28.7 ± 2.7
7	1.0–1.1	$19.36 \pm 0.58 \pm 0.96$	$-26.2 \pm 3.5 \pm 4.8$	19.97 ± 0.34	-15.7 ± 2.6
8	1.1–1.2	$17.81 \pm 0.53 \pm 0.96$	$-18.6 \pm 3.0 \pm 6.1$	18.85 ± 0.30	-6.9 ± 2.0
9	1.2–1.3	$17.70 \pm 0.49 \pm 0.90$	$-13.7 \pm 2.6 \pm 5.1$	19.05 ± 0.27	-1.2 ± 1.6
10	1.3–1.4	$17.72 \pm 0.47 \pm 1.05$	$-8.5 \pm 2.5 \pm 5.8$	19.47 ± 0.25	4.8 ± 1.4
11	1.4–1.5	$17.13 \pm 0.45 \pm 1.05$	$-3.2 \pm 2.4 \pm 4.7$	19.36 ± 0.23	11.6 ± 1.3
12	1.5–1.6	$17.16 \pm 0.45 \pm 1.04$	$0.5 \pm 2.3 \pm 5.6$	19.80 ± 0.22	17.1 ± 1.3
13	1.6–1.7	$17.09 \pm 0.46 \pm 1.14$	$5.4 \pm 2.3 \pm 4.0$	20.35 ± 0.22	24.3 ± 1.3
14	1.7–1.8	$16.94 \pm 0.47 \pm 1.06$	$7.5 \pm 2.3 \pm 4.6$	20.61 ± 0.24	30.1 ± 1.3
15	1.8–1.9	$16.41 \pm 0.48 \pm 1.05$	$9.5 \pm 2.4 \pm 3.7$	20.38 ± 0.27	38.0 ± 1.3
16	1.9–2.0	$15.91 \pm 0.51 \pm 0.75$	$12.3 \pm 2.7 \pm 3.2$	19.86 ± 0.34	49.1 ± 1.4
17	2.0–2.1	$15.97 \pm 0.56 \pm 1.11$	$16.9 \pm 2.9 \pm 3.1$	19.07 ± 0.40	63.4 ± 1.4
18	2.1–2.2	$15.72 \pm 0.61 \pm 1.11$	$15.7 \pm 2.5 \pm 2.2$	14.20 ± 0.40	76.6 ± 1.9
19	2.2–2.3	$16.54 \pm 0.63 \pm 1.17$	$17.3 \pm 2.1 \pm 2.1$	9.29 ± 0.39	75.2 ± 2.6
20	2.3–2.4	$16.64 \pm 0.71 \pm 1.42$	$20.1 \pm 2.1 \pm 3.4$	7.10 ± 0.43	57.5 ± 3.1
21	2.4–2.5	$15.91 \pm 0.86 \pm 1.61$	$19.8 \pm 2.3 \pm 2.0$	6.75 ± 0.43	33.5 ± 3.2
22	2.5–2.6	$17.25 \pm 1.03 \pm 1.83$	$21.5 \pm 2.4 \pm 2.0$	9.46 ± 0.51	26.0 ± 2.5
23	2.6–2.7	$17.24 \pm 1.21 \pm 2.38$	$24.1 \pm 2.6 \pm 2.9$	10.74 ± 0.55	26.7 ± 2.6
24	2.7–2.8	$17.59 \pm 1.34 \pm 2.28$	$29.0 \pm 2.8 \pm 1.6$	12.04 ± 0.64	31.8 ± 2.5
25	2.8–2.9	$16.51 \pm 1.65 \pm 2.56$	$32.7 \pm 3.5 \pm 3.5$	11.79 ± 0.79	36.0 ± 3.3
26	2.9–3.0	$14.07 \pm 3.28 \pm 3.32$	$35.6 \pm 6.0 \pm 3.8$	9.75 ± 2.50	38.6 ± 6.1

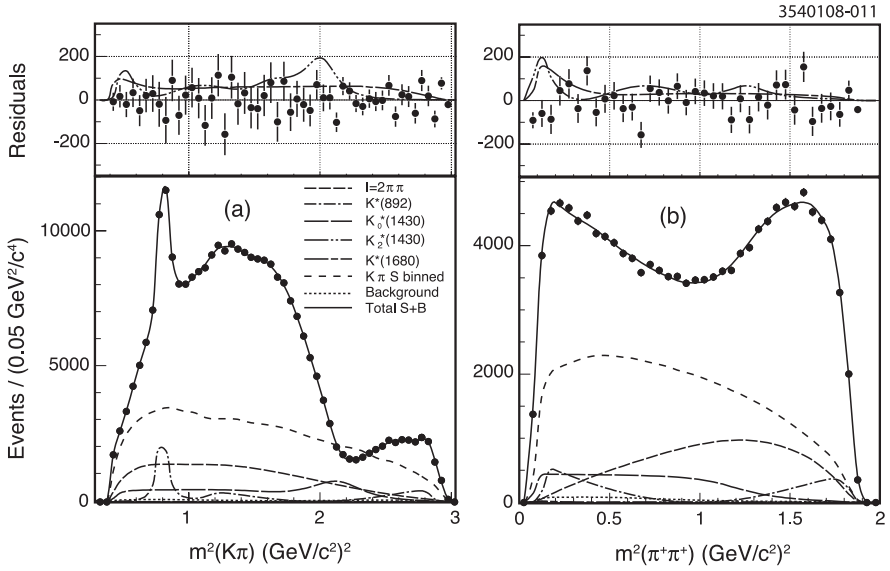

FIG. 10. Projections of the fit to the Dalitz plot with QMIPWA on (a) $m^2(K\pi)$ (two entries per event) and (b) $m^2(\pi\pi)$ variables. Residuals between data and the total p.d.f. are shown by dots with statistical error bars on the top inset along with minor contributions from the $K^*(1680)$ and $K_2^*(1430)$ resonances, plotted with factor $\times 10$.

B. Cross-check for binned $I = 2$ $\pi^+\pi^+$ S wave

In this approach we also check how much the $I = 2$ $\pi^+\pi^+$ S wave might be different from its analytic approximation in model I2. The analytic expression, given in Eq. (26), is replaced by the binned wave from Eq. (29). We fix all 20 fit parameters to their values in model I2.

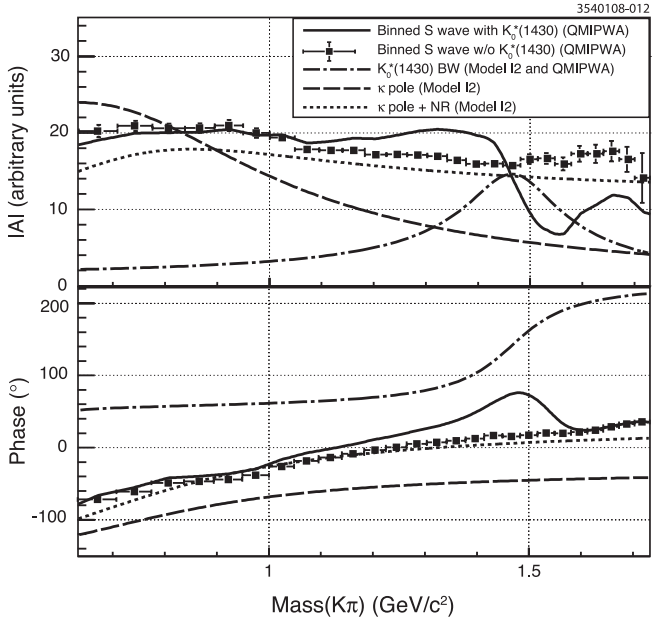

FIG. 11. The magnitude and phase of the $K\pi$ S wave in model I2 and QMIPWA. The dots with error bars for statistical uncertainties and the solid curve show the binned $K\pi$ S wave without $K_0^*(1430)$ and the total $K\pi$ S wave from Table VIII, respectively. Other curves show the S wave components of model I2 with parameters from Table VII.

Then, we fix to zero the magnitude of the analytic $I = 2$ $\pi^+\pi^+$ S wave, $a_{\pi\pi} = 0$, and add a binned $I = 2$ $\pi^+\pi^+$ S wave; the magnitude and phase in each of the 18 bins of $m^2_{\pi^+\pi^+}$ are allowed to float. Results of this fit are shown in Table IX. The measured $I = 2$ $\pi^+\pi^+$ S wave is compared

TABLE IX. QMIPWA: Results for $\pi^+\pi^+$ S wave, which are also shown by dots with error bars in Fig. 12. Variation of the χ^2 and number of degrees of freedom $\Delta\nu$ is shown with respect to model I2.

Bin #	$m^2_{\pi\pi}$ (GeV/c^2)2 Bin range	$I = 2$ $\pi^+\pi^+$ S wave Magnitude (a.u.)	Phase (°)
1	0.1–0.2	3.62 ± 0.44	-113.9 ± 7.0
2	0.2–0.3	4.31 ± 0.37	-115.8 ± 4.7
3	0.3–0.4	4.51 ± 0.33	-120.7 ± 3.6
4	0.4–0.5	6.17 ± 0.33	-116.8 ± 2.4
5	0.5–0.6	6.84 ± 0.34	-118.9 ± 2.1
6	0.6–0.7	8.13 ± 0.35	-121.8 ± 1.8
7	0.7–0.8	7.77 ± 0.35	-121.7 ± 1.9
8	0.8–0.9	8.65 ± 0.35	-125.5 ± 1.7
9	0.9–1.0	8.95 ± 0.37	-126.3 ± 1.6
10	1.0–1.1	9.61 ± 0.42	-127.9 ± 1.5
11	1.1–1.2	11.69 ± 0.55	-127.9 ± 1.3
12	1.2–1.3	10.04 ± 0.93	-132.0 ± 1.5
13	1.3–1.4	12.43 ± 1.01	-131.0 ± 1.2
14	1.4–1.5	12.92 ± 0.98	-131.1 ± 1.3
15	1.5–1.6	9.51 ± 0.98	-131.4 ± 1.8
16	1.6–1.7	11.56 ± 1.00	-134.7 ± 1.8
17	1.7–1.8	11.75 ± 1.10	-142.5 ± 2.1
18	1.8–1.9	10.52 ± 2.02	-156.1 ± 5.2
FF(%)		9.8 ± 0.4	
$\Delta\chi^2/\Delta\nu$		$(390 - 416)/(-36 + 20)$	

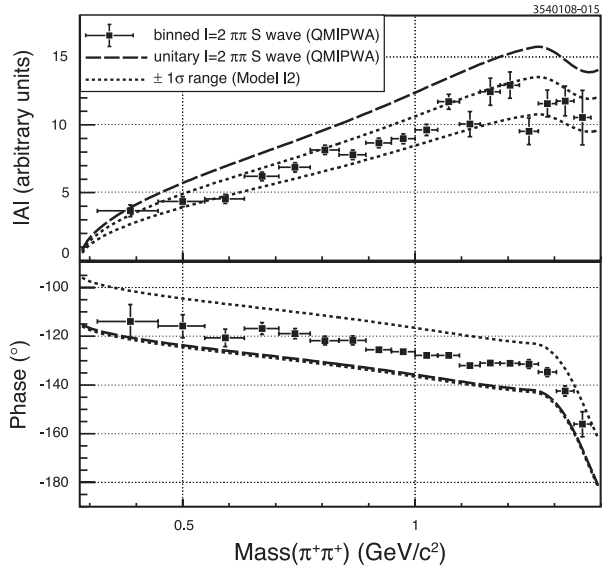

FIG. 12. The magnitude and phase of the $I = 2$ $\pi^+\pi^+$ S wave in model I2 and QMIPWA. The dots with error bars for statistical uncertainties represent results from Table IX. Other curves show the $I = 2$ $\pi^+\pi^+$ S wave of model I2 and QMIPWA with parameters from Table VII.

to the model I2 analytic function in Fig. 12. The change of the χ^2 in this fit compared to model I2, $\Delta\chi^2 = 390 - 416 = -26$, does not show a significant improvement for the change $\Delta\nu = -36 + 20 = -16$ in degrees of freedom due to fixing 20 of the original parameters and introducing 36 new parameters. The data do not prefer the binned amplitude to the analytic model for the $I = 2$ $\pi^+\pi^+$ S wave.

C. Cross-checks for binned $K\pi$ P and D waves

To check how much the P and D waves might be different from their model parametrization we use the same binned technique. All of the fit parameters are fixed to their optimal values from model I2. The P wave binned amplitude substitutes for the smooth $K^*(1680)$ resonance only. The sharp shape of the $K^*(892)$ resonance is accounted for by a Breit-Wigner function. The D wave binned amplitude substitutes for the $K_2^*(1430)$ contribution, even though it is not particularly smooth. The magnitude and phase in 26 bins of $m^2_{K\pi}$ are allowed to float for the P or D wave in two separate fits, respectively. The resolution for the D wave is worse, and we use only 18 bins

TABLE X. Results for $K\pi$ P and D binned waves using model I2, which is also shown by dots with error bars in Figs. 13 and 14, respectively. Variation of the χ^2 and number of degrees of freedom $\Delta\nu$ is shown with respect to model I2. The D wave is used only in the range $[0.9, 2.7]$ $(\mathrm{GeV}/c^2)^2$ as explained in the text.

Bin #	$m^2_{K\pi}$ $(\mathrm{GeV}/c^2)^2$	Binned P wave for $K^*(1680)$		Binned D wave for $K_2^*(1430)$	
	Bin range	Magnitude (a.u.)	Phase (°)	Magnitude (a.u.)	Phase (°)
1	0.4–0.5	1.96 ± 1.26	41.0 ± 28.0	···	···
2	0.5–0.6	2.90 ± 1.12	199.2 ± 11.2	···	···
3	0.6–0.7	0.67 ± 0.93	50.1 ± 15.8	···	···
4	0.7–0.8	0.81 ± 0.36	46.4 ± 18.4	···	···
5	0.8–0.9	0.60 ± 0.35	102.3 ± 33.7	···	···
6	0.9–1.0	0.58 ± 1.36	73.2 ± 25.7	0.71 ± 0.17	-61.8 ± 23.6
7	1.0–1.1	1.87 ± 0.77	79.5 ± 7.01	0.31 ± 0.14	-5.0 ± 69.6
8	1.1–1.2	0.09 ± 0.42	51.7 ± 22.4	0.66 ± 0.16	-15.6 ± 27.2
9	1.2–1.3	1.12 ± 0.38	81.3 ± 10.6	1.14 ± 0.19	-50.0 ± 12.9
10	1.3–1.4	1.49 ± 0.33	74.4 ± 8.79	1.09 ± 0.19	-28.7 ± 13.1
11	1.4–1.5	0.81 ± 0.33	83.9 ± 13.3	0.97 ± 0.19	-9.9 ± 14.2
12	1.5–1.6	1.25 ± 0.33	80.8 ± 10.6	1.30 ± 0.21	-15.5 ± 14.0
13	1.6–1.7	1.30 ± 0.34	73.3 ± 9.79	1.45 ± 0.24	11.6 ± 13.5
14	1.7–1.8	1.77 ± 0.36	77.7 ± 8.34	2.18 ± 0.26	-16.3 ± 10.2
15	1.8–1.9	1.16 ± 0.40	88.1 ± 11.1	3.28 ± 0.28	24.4 ± 7.83
16	1.9–2.0	1.79 ± 0.45	90.9 ± 9.91	5.77 ± 0.38	31.9 ± 5.45
17	2.0–2.1	1.86 ± 0.42	102.1 ± 11.2	4.77 ± 0.52	70.2 ± 5.90
18	2.1–2.2	2.42 ± 0.45	104.3 ± 12.2	4.45 ± 0.70	100.2 ± 7.41
19	2.2–2.3	2.58 ± 0.52	115.7 ± 12.6	4.69 ± 0.97	127.8 ± 8.52
20	2.3–2.4	1.66 ± 0.55	119.6 ± 16.6	3.79 ± 1.13	116.8 ± 16.3
21	2.4–2.5	3.76 ± 0.60	108.8 ± 11.4	0.18 ± 1.42	-3.3 ± 84.7
22	2.5–2.6	4.19 ± 0.75	113.6 ± 13.7	4.86 ± 1.72	135.8 ± 33.2
23	2.6–2.7	6.71 ± 0.98	105.0 ± 16.9	1.54 ± 2.58	184.8 ± 78.5
24	2.7–2.8	3.35 ± 1.59	142.4 ± 29.4	···	···
25	2.8–2.9	7.03 ± 2.49	183.2 ± 22.5	···	···
26	2.9–3.0	32.66 ± 17.9	232.2 ± 11.6	···	···
FF(%), $2\times$		0.20 ± 0.03		0.15 ± 0.01	
$\Delta\chi^2/\Delta\nu$		$(373 - 416)/(-52 + 20)$		$(400 - 416)/(-36 + 20)$	

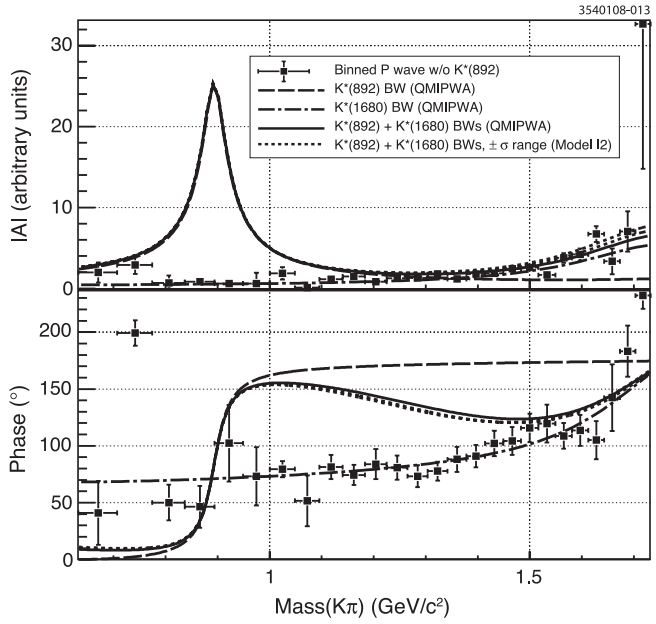

FIG. 13. The magnitude and phase of the $K\pi$ P wave in model I2 and QMIPWA. The dots with error bars for statistical uncertainties represent results from Table X. Other curves show the P wave components of model I2 and QMIPWA with parameters from Table VII.

in the $m^2_{K\pi}$ range $[0.9, 2.7]$ $(\mathrm{GeV}/c^2)^2$. Results of these fits are shown in Table X. The measured P and D binned waves and their comparison with the model I2 components are displayed in Figs. 13 and 14, respectively.

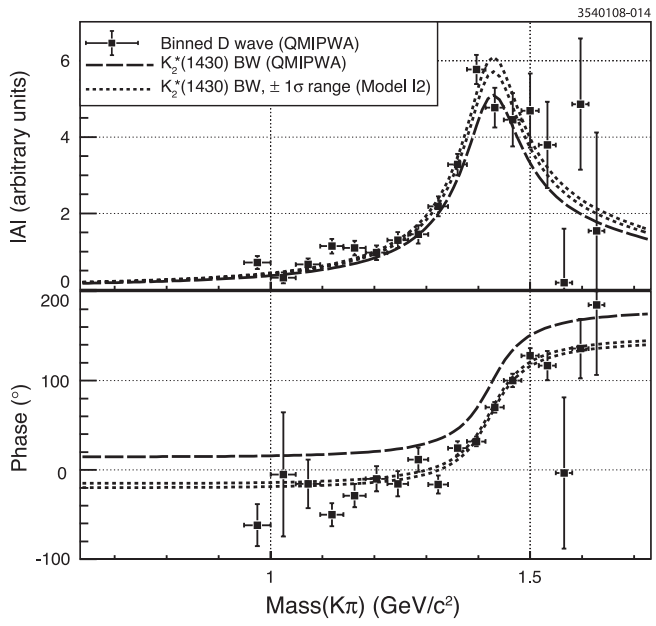

FIG. 14. The magnitude and phase of the $K\pi$ D wave in model I2 and QMIPWA. The dots with error bars for statistical uncertainties represent results from Table X. Other curves show the D wave components of model I2 and QMIPWA with parameters from Table VII.

The relative fraction of the P and especially the D wave is much smaller than the S wave. This explains the poor resolution for these binned amplitudes. We find that our binned P and D waves are consistent with their substituted components in model I2. This cross-check adds some confidence to this quasi-model-independent technique.

VI. CROSS-CHECKS AND SYSTEMATIC UNCERTAINTIES

A. Systematic uncertainties

In order to estimate systematic uncertainties of the fit parameters, we apply numerous variations to the fitting procedure and examine the change of the fit parameters. Because of the numerous variations, a quadratic sum of the resulting small changes due to the variations would lead to a systematic error that is too conservative. Instead, we treat all of the resulting changes from the variations as a frequency distribution and calculate the *mean* and *rms* of the distribution. The *total* systematic uncertainty is obtained as a quadratic sum of the difference between the obtained mean and the default value of that parameter, and the rms.

We consider the six divisions of our sample: splitting events evenly between earlier and later data sets; D^+ and D^- decays; tight $[1\sigma(\Delta E) \times 1\sigma(m_{\mathrm{BC}})]$ and loose $[3\sigma(\Delta E) \times 3\sigma(m_{\mathrm{BC}})]$ signal box cuts. Other systematic variations common to all of the models (model C, model I2, and QMIPWA), are as follows:

(i) Float f_{sig}. We find that it is always consistent with its nominal value of 0.9892.
(ii) Drop the background term and set $f_{\mathrm{sig}} = 1$.
(iii) Float the efficiency coefficients in a simultaneous fit to data and MC samples. In this case variations of the efficiency parameters are constrained by the MC sample.
(iv) Improve the precision of the calculation of the normalization integrals from Eq. (3) by an order of magnitude.

We repeated the fits with the radii for the Blatt-Weisskopf [19] form factors a factor of 2 larger and smaller than their nominal values and found negligible change in the central result.

Depending on the model we apply additional systematic variations, which are also included in systematic uncertainties. In model C and model I2, discussed in Sec. IV, we consider variation of the resonance parameters as follows:

(i) Float parameters of the $K^*(892)$ and $K^*_0(1430)$ resonances. The mass and width are shown in Table IV.
(ii) Float parameters of the $K^*_2(1430)$ or $K^*(1680)$ resonances. The mass and width are shown in Table IV.
(iii) Add a $K^*(1410)$ contribution. We find that it is not significant: $\mathrm{FF}_{K^*(1410)} < 0.1\%$ at 90% C.L.
(iv) In model C we test the event sample selected without a kinematic fit with appropriate coefficients for efficiency and background shapes. We find that the

resulting variation is negligible, and this study is not performed for the other fit models.

(v) In QMIPWA we use the binned $K^-\pi^+$ S wave as a histogram without linear interpolation.

None of these variations reveal an obviously dominant source of systematic uncertainty.

B. Additional cross-checks

Common cross-checks listed below bring us to models that are different enough that we do not include these results in the total systematic uncertainty.

(i) Remove the $K_2^*(1430)$ resonance contribution. We find a significant degradation of the fit quality. For example, $\Delta\chi^2 = 370$ in model C.

(ii) Remove the $K^*(1680)$ resonance contribution. We find a significant degradation of the fit quality. For example, $\Delta\chi^2 = 250$ in model C.

Based on these fits we conclude that the $K_2^*(1430)$ and $K^*(1680)$ resonances cannot be removed. Their contributions are small (FF $< 1\%$) but significant, and the fit quality is very poor without these resonances. We apply a similar backward check for model I2 and QMIPWA:

(i) We remove the $I = 2$ $\pi^+\pi^+$ S wave contribution and get a poor quality fit.

VII. DISCUSSION

A. $K_0^*(1430)$ and $K^*(892)$ parameters

The $K_0^*(1430)$ parameters, which we obtain in fits with the isobar models, listed in Table IV as well as in Tables V, VI, and VII, are consistent with each other and are significantly different from the PDG [1] values which are dominated by the LASS measurement. Our data prefer a $K_0^*(1430)$ resonance that is 50 MeV/c^2 heavier and about 2 times narrower. Our result is consistent with E791 [6] and FOCUS [23] measurements. Possible explanations include that the $K_0^*(1430)$ resonance parameters depend on its production mechanism which are different in $K\pi$ scattering and D-meson decays or that the $K_0^*(1430)$ parameters are strongly model-dependent. In particular, they may depend on interference with other S wave contributions.

In all of our fits, as seen in Tables IV and VII, the $K^*(892)$ parameters are consistent with each other. The measured masses are consistent with the nominal value [1], but the widths are about 5 MeV/c^2 narrower. The $K^*(892)$ width in the PDG is an average value over about 20 experimental measurements. Our measurement does not contradict any single result included in PDG. The largest difference is about 3 standard deviations from the LASS value. We also tested the $K^*(892)$ width model dependence. The largest variation is expected from applying Blatt-Weisskopf form factors. A variation of the radial parameters from zero to 4 times their nominal values causes a variation in the width of 0.7 MeV/c^2, which cannot explain the large difference with the PDG average. Recent results from FOCUS [24] and Belle [25] also indicate a $K^*(892)$ width smaller than the PDG value.

B. Partial waves

The factorized Gaussian form factors used in model C for the $K\pi$ S wave components may cause an enhancement of the complex function magnitude at low $K\pi$ mass, as mentioned in Sec. IV B. However, the form factor is a real function and does not change the phase of the complex S wave. In model I2 and QMIPWA we measure the total $K\pi$ S wave amplitude without using a form factor. It means that the measured S wave absorbs the form factor. The measured S wave magnitude is essentially constant up to 1.4 GeV/c^2, as demonstrated in Fig. 11. The phase of the complex S wave amplitude shows smooth variation from $-80°$ at $K\pi$ threshold to $40°$ at 1.4 GeV/c^2. At higher mass the amplitude is distorted by a contribution from the $K_0^*(1430)$ resonance. Our data require a dominant contribution from the $K\pi$ S wave, which at low mass is not well described as a regular resonance structure.

In QMIPWA the S wave is measured in a model-independent way, while the P and D waves are parametrized by Breit-Wigner resonances. In cross-checks we add more freedom to the P and D waves by replacing the $K^*(1680)$ and $K_2^*(1430)$, respectively, Breit-Wigner shapes with the binned amplitudes, as illustrated in Figs. 13 and 14. We did not find improvement in the fit quality or any significant deviation of the binned wave from the analytic function of the isobar model. The systematic uncertainties described above are larger than variations caused by the possible model dependence of the P and D waves.

In model I2 and QMIPWA we find that the $I = 2$ $\pi^+\pi^+$ S wave amplitude is not consistent with a constant term as seen in Fig. 12. Its behavior is well modeled by the analytic function [Eq. (26)]; the binned wave also describes the behavior consistently.

C. Comparison of fit models

Note that in model C, model I2, and QMIPWA (Tables IV, V, VI, and VII) the magnitudes and phases for the resonance contributions $K^*(892)$ (by construction), $K_0^*(1430)$, $K_2^*(1430)$, and $K^*(1680)$ are consistent. On the other hand, the fit fractions for the resonances differ significantly among the models. The differences in fit fractions arise from our models of the $K\pi$ S wave and the $I = 2$ $\pi^+\pi^+$ S wave when it is included. Indeed, in model C the $K\pi$ S wave amplitude is represented by the NR term and a broad Breit-Wigner resonance for the κ. They have small magnitudes, and they interfere constructively. This leads to small fit fractions, and the sum of all fit fractions is less than 100%. In model I2 the $K\pi$ S wave amplitude is represented by the NR term and the complex pole for the κ. The $I = 2$ $\pi^+\pi^+$ S wave is also included in this model. These amplitudes are large, and they interfere destructively. This leads to large fit fractions, and the sum

of all fit fractions is greater than 100%. Both models describe the total $K\pi$ S wave with complex functions that qualitatively show very similar behavior. However, the fit fractions, especially for the components of the $K\pi$ S wave, strongly depend on the assumed composition of this amplitude.

In contrast the QMIPWA represents the $K\pi$ S wave amplitude as a single function. We make no assumptions about the composition of the $K\pi$ S wave in this case. It also includes the $I = 2$ $\pi^+\pi^+$ S wave, which plays a key role in improving the fit quality. We feel this approach is the most reliable presentation of results for the fit fractions for resonance and S wave contributions to the $D^+ \to K^-\pi^+\pi^+$ decay.

VIII. SUMMARY

We describe a partial wave analysis of the $D^+ \to K^-\pi^+\pi^+$ events on the Dalitz plot. We use the CLEO-c data set of 572 pb^{-1} of e^+e^- collisions accumulated at the $\psi(3770)$, which corresponds to a sample of 1.6×10^6 D^+D^- pairs produced in the process $e^+e^- \to \psi(3770) \to D^+D^-$. We select 140 793 candidate events for the Dalitz plot with a small background of 1.1%. We compare our results with the best previous measurements from E791 [6] using the isobar model. Our results agree with the E791 measurement, as shown in Table V for their best model. The fit quality can be improved if we add the $I = 2$ $\pi^+\pi^+$ S wave contribution, as presented in Table VII.

We apply a model-independent approach, developed in Ref. [7], to measure the magnitude and phase of the $K\pi$ S wave in the invariant mass range from threshold to the maximum value in this decay. In contrast to E791, we have measured the $K\pi$ S wave without factorization of the form factor for scalar resonances. Our results on the $K\pi$ S wave phase and magnitude measurement are presented in Table VIII and in Fig. 11. The accuracy of the $K\pi$ S wave measurement is improved, compared to the only previous measurement [7]. We find that the total observed S wave magnitude in the $D^+ \to K^-\pi^+\pi^+$ decay is essentially constant from $K\pi$ production threshold to 1.4 GeV/c^2. The phase shows smooth variation from $-80°$ to $40°$ in the same range. At higher invariant mass $m_{K\pi} > 1.4$ GeV/c^2, the S wave behavior is dominated by the $K_0^*(1430)$ resonance. We find that the P wave contribution is dominated by $K^*(892)$ and $K^*(1680)$ Breit-Wigner resonances, and the D wave has only a contribution from $K_2^*(1430)$. Using binning techniques, we find no significant deviation of the P and D waves from the isobar model, as demonstrated in Figs. 13 and 14.

In the model-independent approach for the $I = 2$ $\pi^+\pi^+$ S wave we obtain the binned amplitude parameters, listed in Table IX and shown in Fig. 12, which are consistent with the analytic form of this wave. We find that the $I = 2$ $\pi^+\pi^+$ S wave has a nonuniform variation in the amplitude across the $m(\pi^+\pi^+)$ kinematic range with a fit fraction of 10%–15%. As expected, the measured amplitude behavior and the fit fraction of the $K\pi$ S wave changes slightly with the addition of the $I = 2$ $\pi^+\pi^+$ S wave. The addition of the $I = 2$ $\pi^+\pi^+$ S wave to either the isobar model or the model-independent partial wave approach is the key piece that gives good agreement with the data in both cases.

ACKNOWLEDGMENTS

We gratefully acknowledge the effort of the CESR staff in providing us with excellent luminosity and running conditions. D. C.-H. and A. R. thank the A. P. Sloan Foundation. This work was supported by the National Science Foundation, the U.S. Department of Energy, the Natural Sciences and Engineering Research Council of Canada, and the U.K. Science and Technology Facilities Council.

APPENDIX: KINEMATIC VARIABLES AND ANGULAR DISTRIBUTIONS

Following previous CLEO analyses (see, for example, Ref. [18]) we use the angular distributions [Eqs. (10)–(12)] obtained from a covariant-tensor formalism. The E791 form [7] was applied to the orbital momentum partial wave decomposition using the term $(-2\mathrm{P}_a\mathrm{P}_c)^L\mathcal{P}_L(\cos\theta)$ instead of $\Omega_L(s, t)$ in Eq. (9). Here $\mathcal{P}_L(\cos\theta)$ is a Legendre polynomial, P_a, P_c, and θ are the momenta and the angle between particles a and c in the resonance R rest frame, respectively. In this section we show that both approaches are equivalent up to constant coefficients. As a by-product we also obtain expressions for the decay momenta used in the Blatt-Weisskopf form factors [Eqs. (13)–(16)].

The kinematic variables in the decay under study, schematically shown in Fig. 6, can be expressed in terms of invariant variables (masses and invariant masses) in the decaying particle d (D^+ meson) or resonance R rest frames. The energy and momentum of particle a in the resonance R or (ab) rest frame can be obtained from the 4-momentum balance equation $p_b = p_R - p_a$, where $p_R = (m_{ab}, \vec{0})$ and $p_a = (E_a, \mathbf{P}_a)$. Then, $p_b^2 = m_b^2 = m_{ab}^2 + m_a^2 - 2m_{ab}E_a$, giving the energy

$$E_a = \frac{m_{ab}^2 + m_a^2 - m_b^2}{2m_{ab}} \tag{A1}$$

and relevant momentum squared

$$\mathrm{P}_a^2 = E_a^2 - m_a^2 = \frac{1}{4}\left(m_{ab}^2 - 2m_a^2 - 2m_b^2 + \frac{(m_a^2 - m_b^2)^2}{m_{ab}^2}\right). \tag{A2}$$

The energy and momentum of the particle c in the resonance R rest frame can be obtained from the particle d invariant mass squared $m_d^2 = (p_c + p_R)^2$. In the resonance rest frame $p_c = (E_c, \mathbf{P}_c)$ and $p_R = (m_{ab}, \vec{0})$, and therefore $m_d^2 = m_c^2 + m_{ab}^2 + 2m_{ab}E_c$, from which we find its energy

$$E_c = \frac{m_d^2 - m_{ab}^2 - m_c^2}{2m_{ab}} \tag{A3}$$

and the associated momentum squared

$$\mathrm{P}_c^2 = E_c^2 - m_c^2 = \frac{1}{4}\left(m_{ab}^2 - 2m_d^2 - 2m_c^2 + \frac{(m_d^2 - m_c^2)^2}{m_{ab}^2}\right). \tag{A4}$$

The energy and momentum of the same particle c in the D meson rest frame, denoted here by the asterisk, have different expressions:

$$E_c^* = \frac{m_d^2 - m_{ab}^2 + m_c^2}{2m_d}, \qquad \mathrm{P}_c^{*2} = E_c^{*2} - m_c^2. \tag{A5}$$

The angular distributions in the E791 [7] analysis are defined by the Legendre polynomials $\mathcal{P}_L(\cos\theta)$:

$$\mathcal{P}_0(x) = 1, \qquad \mathcal{P}_1(x) = x, \qquad \mathcal{P}_2(x) = \frac{3x^2 - 1}{2}, \qquad \mathcal{P}_3(x) = \frac{5x^3 - 3x}{2}, \ldots, \tag{A6}$$

where θ is the angle between particles a and c in the resonance R rest frame. This $\cos\theta$ can be expressed through the known energies and momenta of particles a and c and their measured invariant mass squared $m_{ac}^2 = (p_a + p_c)^2 = m_a^2 + m_c^2 + 2E_aE_c - 2\mathrm{P}_a\mathrm{P}_c\cos\theta$, so

$$\cos\theta = \frac{m_a^2 + m_c^2 + 2E_aE_c - m_{ac}^2}{2\mathrm{P}_a\mathrm{P}_c}. \tag{A7}$$

Substituting E_a and E_c from Eqs. (A1)–(A3) in the numerator of Eq. (A7) we get

$$\cos\theta = \frac{1}{4\mathrm{P}_a\mathrm{P}_c}\left(m_{bc}^2 - m_{ac}^2 + \frac{(m_d^2 - m_c^2)(m_a^2 - m_b^2)}{m_{ab}^2}\right). \tag{A8}$$

Note that these angular distributions are equivalent to formulas used in Eqs. (10)–(12) up to constant factors. Indeed, comparing the expressions for $(-2\mathrm{P}_a\mathrm{P}_c)^L\mathcal{P}_L(\cos\theta)$ from Ref. [7] with Ω_L we get

$$(-2\mathrm{P}_a\mathrm{P}_c)^0\mathcal{P}_0(\cos\theta) = 1 = \Omega_{L=0}, \tag{A9}$$

$$(-2\mathrm{P}_a\mathrm{P}_c)^1\mathcal{P}_1(\cos\theta) = -2\mathrm{P}_a\mathrm{P}_c\cos\theta = \tfrac{1}{2}\Omega_{L=1}, \tag{A10}$$

$$(-2\mathrm{P}_a\mathrm{P}_c)^2\mathcal{P}_2(\cos\theta) = 4(\mathrm{P}_a\mathrm{P}_c)^2\frac{3\cos^2\theta - 1}{2} = \frac{3}{8}\Omega_{L=2}. \tag{A11}$$

[1] W.-M. Yao *et al.*, J. Phys. G **33**, 1 (2006).
[2] J. Adler *et al.* (MARK III Collaboration), Phys. Lett. B **196**, 107 (1987).
[3] M. P. Alvarez *et al.* (NA14/2 Collaboration), Z. Phys. C **50**, 11 (1991).
[4] J. C. Anjos *et al.* (E691 Collaboration), Phys. Rev. D **48**, 56 (1993).
[5] P. L. Frabetti *et al.* (E687 Collaboration), Phys. Lett. B **331**, 217 (1994).
[6] E. M. Aitala *et al.* (E791 Collaboration), Phys. Rev. Lett. **89**, 121801 (2002).
[7] E. M. Aitala *et al.* (E791 Collaboration), Phys. Rev. D **73**, 032004 (2006).
[8] R. H. Dalitz, Philos. Mag. **44**, 1068 (1953).
[9] D. Bugg, arXiv:hep-ex/0510014.
[10] D. Bugg, Phys. Lett. B **632**, 471 (2006).
[11] J. A. Oller, Phys. Rev. D **71**, 054030 (2005).
[12] W. Hoogland *et al.*, Nucl. Phys. **B126**, 109 (1977); N. B. Durusoy *et al.*, Phys. Lett. **45B**, 517 (1973); B. S. Zou *et al.*, in *Proceedings of the Tenth International Conference on Hadron Spectroscopy*, edited by E. Klempt, H. Koch, and H. Orth, AIP Conf. Proc. No. 717 (AIP, New York, 2004), pp. 347–351.
[13] G. Viehhauser, Nucl. Instrum. Methods Phys. Res., Sect. A **462**, 146 (2001); D. Peterson *et al.*, Nucl. Instrum. Methods Phys. Res., Sect. A **478**, 142 (2002); Y. Kubota *et al.*, Nucl. Instrum. Methods Phys. Res., Sect. A **320**, 66 (1992); R. A. Briere *et al.* (CESR-c and CLEO-c Taskforces, CLEO-c Collaboration), Cornell University, LEPP Report No. CLNS 01/1742, 2001 (unpublished).
[14] S. Dobbs *et al.* (CLEO Collaboration), Phys. Rev. D **76**, 112001 (2007).
[15] H. Albrecht *et al.*, Phys. Lett. B **229**, 304 (1989).
[16] G. Bonvicini *et al.* (CLEO Collaboration), Phys. Rev. D **76**, 012001 (2007).
[17] D. J. Lange, Nucl. Instrum. Methods Phys. Res., Sect. A **462**, 152 (2001).
[18] S. Kopp *et al.* (CLEO Collaboration), Phys. Rev. D **63**, 092001 (2001).
[19] J. M. Blatt and V. F. Weisskopf, *Theoretical Nuclear Physics* (Wiley, New York, 1951), p. 361.
[20] N. A. Tornqvist, Z. Phys. C **68**, 647 (1995).
[21] N. N. Achasov and G. N. Shestakov, Phys. Rev. D **67**, 114018 (2003).
[22] D. E. Groom *et al.*, Eur. Phys. J. C **15**, 1 (2000).
[23] J. M. Link *et al.* (FOCUS Collaboration), Phys. Lett. B **653**, 1 (2007).
[24] J. M. Link *et al.* (FOCUS Collaboration), Phys. Lett. B **621**, 72 (2005).
[25] D. Epifanov *et al.* (Belle Collaboration), Phys. Lett. B **654**, 65 (2007).